

A Heteroclinic Connection between Two Saddle Slow Manifolds in the Olsen Model

Elle Musoke, Bernd Krauskopf, and Hinke M. Osinga

Department of Mathematics, University of Auckland, Private Bag 92019

Auckland, 1142, New Zealand

elle.musoke@auckland.ac.nz

Received (to be inserted by publisher)

The abstract should summarize the context, content and conclusions of the paper. It should not contain any references or displayed equations. Typeset the abstract in 10 pt Times Roman with baselineskip of 12 pt, making an indentation of 1.6 cm on the left and right margins.

Keywords: A list of 3–5 keywords are to be supplied.

1. Introduction

Multiple-time scale dynamical systems are characterized by certain variables evolving on a fast time scale while other variables evolve on a slower time scale. The separation of variables into fast and slow can be found in many systems: chemical systems, neurons, electric circuits, lasers, and predator-prey dynamics, among others, have been described by slow-fast models [Brøns & Bar-Eli, 1991; De Maesschalck & Wechselberger, 2015; Van der Pol, 1927; Otto *et al.*, 2012; Piltz *et al.*, 2017]. In [Brøns & Bar-Eli, 1991], oscillations in the Belousov-Zhabotinsky reaction are investigated. The geometry of the oscillations arise as a consequence of a time-scale splitting in the variables. Slow-fast models for neurons are studied in [De Maesschalck & Wechselberger, 2015] in which excitability is the result of different time scales. Oscillations are also studied and explained by time-scale splitting in [Van der Pol, 1927]. A slow-fast system is used to model semi-conductor lasers in [Otto *et al.*, 2012]. The role of the length of interspike intervals is investigated. In [Piltz *et al.*, 2017], a slow-fast model is used to investigate the effect of a changing predator diet on predator-prey dynamics. By reason of their ubiquity, various phenomena that arise from the multiple-time-scale nature of slow-fast systems are of significant interest. These have been described for two- and three-dimensional systems by well-established theory [Benoît *et al.*, 1981; Benoît, 1982, 1985; Guckenheimer, 1985; Brøns *et al.*, 2006; Krupa *et al.*, 2008].

We are concerned here with mechanisms responsible for the oscillatory behaviours exhibited by many slow-fast systems. In two-dimensional systems canard explosions, small-amplitude limit cycles transitioning to larger-amplitude relaxation oscillations were studied, for example, in the Van der Pol oscillator and the FitzHugh–Nagumo model [Benoît *et al.*, 1981; FitzHugh, 1955]. In three-dimensional systems, periodic orbits with epochs of localized small-amplitude oscillations (SAOs) and epochs of large-amplitude oscillations (LAOs) have been observed [Hudson *et al.*, 1979]. The mechanisms that cause SAOs of these appropriately named mixed-mode oscillations (MMOs) are described in [Desroches *et al.*, 2012] for three-dimensional systems. In this paper, we investigate novel phenomena that arise in four-dimensional slow-fast systems which may provide insight into undiscovered mechanisms for MMOs in higher-dimensional systems.

Previous studies exploring the mechanisms for MMOs in slow-fast dynamical systems investigate the role of so-called slow manifolds in the MMOs' generation and organisation. Slow manifolds are families of trajectories on which the flow evolves on the slow timescale. A slow manifold may have families of trajectories that converge toward it in forward or backward time, respectively called the stable and unstable manifolds of the slow manifold. If a slow manifold has both a stable and an unstable manifold, it is called a saddle slow manifold. Endocrine pituitary cells were studied with a four-dimensional slow-fast model that had a two-dimensional slow manifold in [Vo *et al.*, 2013b]. In [Harvey *et al.*, 2010] a three-dimensional slow manifold was studied in a four-dimensional model for calcium oscillations inside cells. In [Vo *et al.*, 2013a] a four-dimensional model for a pituitary lactotrophic cell was investigated from both a two- and three-timescale viewpoints. From the two-timescale perspective, the model has a three-dimensional slow manifold. In [Mitry *et al.*, 2013] a six-dimensional model for an excitable neuron was investigated. The model had a two-dimensional slow manifold which played a role in the generation of oscillations in the system. A five-dimensional model with a one-dimensional slow manifold was also investigated. In [Farjami *et al.*, 2018] techniques were developed to compute stable and unstable manifolds of one-dimensional saddle slow manifolds in three-dimensional systems. In [Hasan *et al.*, 2018], these techniques were generalised to compute a two-dimensional saddle slow manifold and its two-dimensional stable and unstable manifolds in the four-dimensional Hodgkin–Huxley model. To our knowledge, there is no literature on the computation of three-dimensional (un)stable manifolds of saddle slow manifolds at this time.

We consider a prototypical four-dimensional slow-fast dynamical system that exhibits MMOs, namely an Olsen model for peroxidase-oxidase reaction. First introduced by Lars F. Olsen in 1983 [Olsen, 1983], there are currently many different versions of the Olsen model of different dimensions. We consider the Olsen model in the form from by [Kuehn & Szmolyan, 2015] and earlier work. The MMO in the Olsen model phase space is of particular interest because it does not seem to be generated by the mechanisms for MMOs familiar from three-dimensional systems.

The classification of variables into those that evolve on a fast time scale and those that evolve on a slow time scale is not straightforward for the Olsen model because the variables are not consistently slow or fast over all regions of phase space. In fact, the Olsen model nominally has three different time scales. We focus specifically on a parameter regime corresponding to two different time scales with three fast and one slow variables. This parameter regime was also the focus in [Desroches *et al.*, 2009] that reports on a study of mechanisms for MMOs after a model reduction to a three-dimensional system. Two saddle slow manifolds were computed along with their stable and unstable manifolds. These gave insight into the formation of the Olsen model MMO, as well as the cause of its particular geometry. However, because of the assumptions used to reduce the model to a three-dimensional system, the dimensions of the stable manifold of one slow manifold and unstable manifold of the other were reduced to two in contrast to the corresponding three-dimensional manifolds in the full system.

In the full system, the three-dimensional stable manifold of one slow manifold and the unstable manifold of the other are expected to intersect generically in a two-dimensional surface of connections between the two slow manifolds. Such a surface does not generically exist in four-dimensional systems for slow manifolds of dimension larger than one. The surface of connections also does not exist generically in systems of dimension lower than four. In these cases, the stable and unstable manifolds of the saddle slow manifolds are limited to dimensions of two or lower and therefore do not typically have robust intersections of dimension two or higher. In this research, we generalise the techniques in [Farjami *et al.*, 2018] with the aim of computing the three-dimensional stable and unstable manifolds of the one-dimensional saddle slow manifolds in the Olsen model. Furthermore, we use our techniques in conjunction with Lin's method to compute the intersection of the three-dimensional stable and unstable manifolds in the full four-dimensional model. This intersection is involved in the formation and organisation of an attracting MMO in our system and could lead to insights about the formation and organisation of MMOs in other higher-dimensional systems.

This paper is organized as follows. In the next section we give the necessary background from geometric singular perturbation theory (GPST) for defining the three-dimensional manifolds which are the focus of this research. Section 3 gives definitions of the manifolds which are then computed in section 4. In section 5, a computation of the intersection of the manifolds computed in section 4 is described. Conclusions are

given in section 6.

2. The Olsen Model

We consider the scaled system from [Kuehn & Szmolyan, 2015], given as the system of ordinary differential equations

$$\begin{cases} \frac{dA}{dt} = \mu - \alpha A - ABY, \\ \frac{dB}{dt} = \varepsilon(1 - BX - ABY), \\ \frac{dX}{dt} = \lambda(BX - X^2 + 3ABY - \zeta X + \delta), \\ \frac{dY}{dt} = \kappa\lambda(X^2 - Y - ABY), \end{cases} \quad (1)$$

where $(A, B, X, Y) \in \mathbb{R}^4$ are positive concentrations of chemicals. The system parameters are represented by the Greek letters appearing in (1) and these have the values given in Table 1. With the minor modification, for notational convenience, of using ε for ε_B and $\frac{1}{\lambda}$ for ε^2 , they are chosen to be as in [Kuehn & Szmolyan, 2015]. The time-scaling parameters ε and λ are chosen so that we are dealing with a regime with three fast variables, A , X , and Y , and one slow variable, B .

Table 1. Parameters of system (1) as in [Kuehn & Szmolyan, 2015] so that (A, X, Y) are fast and (B) is slow.

α	δ	ε	λ	κ	μ	ζ
0.0912	1.2121×10^{-4}	0.0037	18.5281	3.7963	0.9697	0.9847

The classical analysis of slow-fast systems considers the two singular limits, for example [Desroches *et al.*, 2012]. In the limit of $\varepsilon = 0$, system (1) reduces to

$$\begin{cases} \frac{dA}{dt} = \mu - \alpha A - ABY, \\ \frac{dX}{dt} = \frac{1}{\lambda}(BX - X^2 + 3ABY - \zeta X + \delta), \\ \frac{dY}{dt} = \frac{\kappa}{\lambda}(X^2 - Y - ABY), \end{cases} \quad (2)$$

with $\frac{dB}{dt} = 0$, meaning that B is a parameter of (2). We refer to the three-dimensional system (2) as the fast subsystem. Performing the time rescaling $\tau = \varepsilon t$ and then considering the limit of $\varepsilon = 0$, system (1) reduces to the differential algebraic reduced system

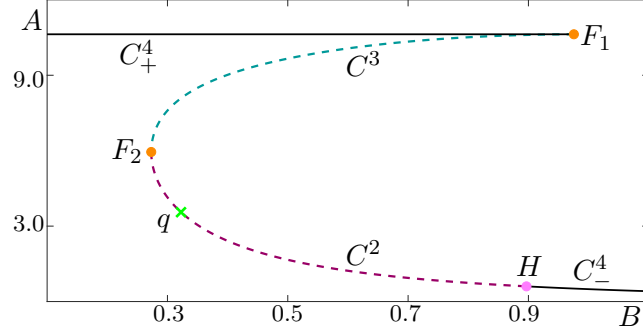


Fig. 1. Physically relevant branches C^2 , C^3 , C_{\pm}^4 of the critical manifold of (1) shown in projection onto the (B, A) -plane. Branches C^2 (raspberry curve) and C^3 (teal curve) consist of saddles of (2) and C_{\pm}^4 (black curve) consist of stable equilibria of (2). Superscripts indicate the number of stable directions possessed by a single equilibrium on a branch and subscripts are used to distinguish between the two branches of stable equilibria. Branches are divided by saddle-node bifurcation points F_1 and F_2 (orange dots) and a Hopf point H (pink dot). Also shown is a saddle equilibrium q (green cross) of (1) existing on C^2 . Parameters are as in Table 1.

$$\begin{cases} 0 & = \mu - \alpha A - ABY, \\ \frac{dB}{d\tau} & = (1 - BX - ABY), \\ 0 & = \frac{1}{\lambda}(BX - X^2 + 3ABY - \zeta X + \delta), \\ 0 & = \frac{\kappa}{\lambda}(X^2 - Y - ABY). \end{cases} \quad (3)$$

The three algebraic equations in system (3) define a one-dimensional manifold, called the critical manifold, denoted C .

The critical manifold C consists of equilibria of the fast subsystem (2), which exist in (A, B, X, Y) -space for different values of B . Their stability can be determined from the eigenvalues of the 3×3 Jacobian matrix of (2) evaluated at each point on the critical manifold. Points $p \in C$ at which the Jacobian of (2) has eigenvalues with non-zero real parts are called hyperbolic. The eigenvectors associated with the eigenvalues are categorized based on the sign of the real part of the associated eigenvalue. Eigenvectors whose associated eigenvalues have negative real parts are called stable directions of p and these span the stable eigenspace $E^s(p)$ of p . The unstable directions and the unstable eigenspace, $E^u(p)$, can be defined similarly by the eigenvectors associated with eigenvalues having positive real part. Note that the dimensions of the stable and unstable eigenspaces are equal to the number of eigenvalues with negative and positive real parts respectively. Equilibria at which the Jacobian has eigenvalues with zero real-part are called non-hyperbolic and these correspond to bifurcations of system (2) (there are lots of introductory ODEs books, are you particular about which one I reference).

The critical manifold C in (A, B, X, Y) -space is divided into branches by bifurcation points of the fast subsystem (2), so that points on each branch have the same dimensions of stable and unstable eigenspaces. In other words, the branches of C are one-parameter families in B of hyperbolic equilibria of system (2). In our notation for branches, superscripts indicate the dimension in (A, B, X, Y) -space of the stable eigenspace of the branch, which are defined as the collection of stable eigenspaces of all the points on the branch. The dimension of the stable eigenspaces of the branches is, hence, one plus than the dimension of the stable eigenspace of each point on the branch. Further, we use subscripts to distinguish the two branches on which equilibria have three-dimensional stable eigenspaces; i.e. are attracting.

Four branches of the critical manifold lie in the physically relevant region where all phase-space variables are positive, these are shown in Figure ?? projected into the (B, A) -plane. The uppermost, black branch, denoted C_{+}^4 , consists of stable equilibria of (2). It is separated from the teal-colored branch of saddle

equilibria, denoted C^3 , by a very sharp fold point F_1 at $B \approx 0.956$ (orange dot). Folds in the critical manifold correspond to saddle-node bifurcations of system (2) with respect to the parameter B , these are points at which one of the real eigenvalues of the Jacobian evaluated at the point switches signs. Another fold at $B \approx 0.273$ denoted F_2 (orange dot), separates C^3 from a lower raspberry-colored branch of saddle equilibria, denoted C^2 . The branch C^2 ends at a Hopf bifurcation H (pink dot) at $B \approx 0.897$, where two complex-conjugate eigenvalues of the Jacobian pass through the imaginary axis of the complex plane. To the right of H , there is again a stable branch of equilibria denoted C^4 .

The point q on C^2 at $B \approx 0.323$ is an equilibrium of system (3) and is, hence, an equilibrium for the full system (1). The equilibrium q has a two-dimensional stable and two-dimensional unstable manifold that are denoted $W^s(q)$ and $W^u(q)$, respectively. The manifolds $W^s(q)$ and $W^u(q)$ can be computed with the methods in [Krauskopf *et al.*, 2007]. To the right of $W^u(q)$ in the (B, A) -projection of Figure ??, the flow is from right to left near C^2 in the full system (1). To the left of $W^u(q)$ the flow is from left to right near C^2 .

Our interest is in the branches C^3 and C^2 because they are saddle objects of different type and are crucial for organising the phase space. These branches of the critical manifold are invariant for $\varepsilon = 0$, but not for $\varepsilon > 0$. However, they do persist as locally invariant manifolds called slow manifolds [Fenichel, 1979]. The associated slow manifolds are traditionally denoted by S_ε^3 and S_ε^2 but, for notational convenience, we drop the subscript indicating dependence on ε and refer to these slow manifolds for $\varepsilon > 0$ simply as S^3 and S^2 . The slow manifold S^3 has the same dimension and stability and lies at an $O(\varepsilon)$ Hausdorff distance from C^3 . In particular, S^3 converges to C^3 as $\varepsilon \rightarrow 0$. (For a definition of Hausdorff distance, see e.g. [Rockafellar & Wets, 2009].) Orbit segments that lie on a slow manifold remain slow for $O(1)$ time with respect to the slow time scale. It follows that any trajectory that remains slow for an $O(1)$ amount of slow time can be considered (to be on) a slow manifold. However, eventually trajectories on a slow manifold may become fast. Due to their finite time nature, slow manifolds are not unique; however, any two slow manifolds lie exponentially close to each other in a suitable $O(\varepsilon)$ neighbourhood of C ???. To select a unique representative S^3 and S^2 , we consider the slow manifold that remains slow for the longest amount of time.

The Stable Manifold Theorem tells us that each $p \in C^3$ has a stable and an unstable manifold that are tangent to and have the same dimensions as $E^s(p)$ and $E^u(p)$, respectively. We denote the stable manifold of a point $p \in C^3$ by $W^s(p)$ and its unstable manifold by $W^u(p)$. The manifolds $W^s(p)$ and $W^u(p)$ consist of trajectories in (A, B, X, Y) -space that converge to p in forward and backward time respectively. We can then define the collection of stable manifolds for $p \in C^3$ as $W^s(C^3) = \bigcup_{p \in C^3} W^s(p)$, which a three-dimensional manifold. We can similarly define the three-dimensional unstable manifold $W^u(C^2)$ of C^2 .

According to Fenichel Theory, for $\varepsilon > 0$, the manifold $W^s(C^3)$ also persists in an $O(\varepsilon)$ neighbourhood as a three-dimensional local stable manifold $W_{loc}^s(S^3)$ of S^3 . The local stable manifold $W_{loc}^s(S^3)$ consists of families of trajectories that have a fast approach to S^3 then remain close to S^3 for $O(1)$ slow time. The three-dimensional unstable manifold $W^u(S^2)$ associated with S^2 is similarly defined for backwards time. Again, due to the finite-time nature of the definitions for the three-dimensional manifolds $W^s(S^3)$ and $W^u(S^2)$, they are not unique. To select unique representatives, we consider two-parameter families of orbit segments that remain slow for the longest amount of time subject to boundary conditions described in further sections.

3. Computation of saddle slow manifolds and their (un)stable manifolds

The definition of a one-dimensional saddle slow manifold and its (un)stable manifolds are given in [Farjami *et al.*, 2018] which presents algorithms for their computation in a three-dimensional system. We are going to define only a unique representative of S^3 associated with C^3 ; the slow manifold S^2 can be defined in a similar manner.

3.1. Definition of S^3

The precise definition of the slow manifold S^3 is given with respect to a closed interval $[B_{\text{in}}, B_{\text{out}}]$ for the slow variable B . The values for B_{in} and B_{out} are chosen such that the interval is contained in the interval

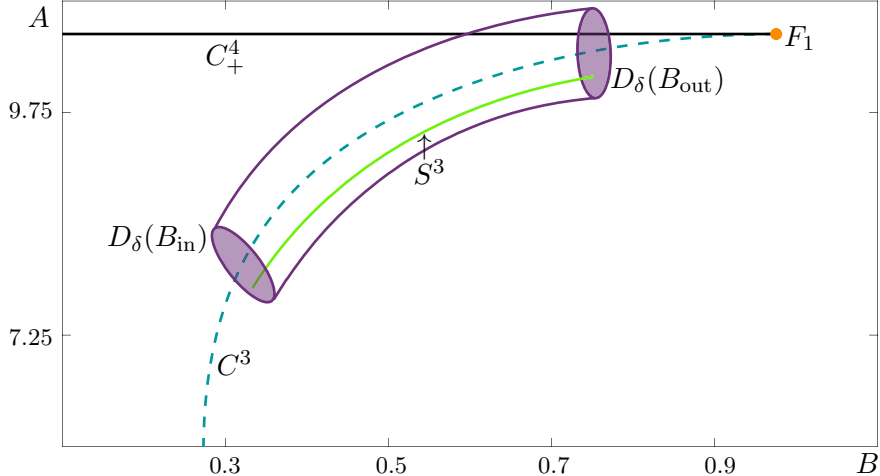


Fig. 2. A sketch of the unique representative slow manifold S^3 (green curve) projected into the (B, A) -plane. The representative slow manifold S^3 is defined by having the longest integration time while entering and exiting $D_\delta(B_{\text{in}})$ and $D_\delta(B_{\text{out}})$ (purple disks) at either end of a four-dimensional cylinder. Also shown are C^3 , C_+^4 , and F_1 .

defined by the B -coordinates of the two fold points F_1 and F_2 . Note that there is a segment in C^3 for which each point $p \in C^3$ is uniquely associated via its B -coordinate with a value $B_p \in [B_{\text{in}}, B_{\text{out}}]$. Hence, for each $B_p \in [B_{\text{in}}, B_{\text{out}}]$ there is a unique point $p = (p_A, p_B, p_X, p_Y) \in C^3$ such that $p_B = B_p$. In the three-dimensional subsection $\{(A \ B \ X \ Y) \in \mathbb{R}^4 \mid B = p_B\}$ we define a solid three-sphere $D_\delta(B_p)$ with radius δ and centre p , given formally by

$$D_\delta(B_p) = \{w \in \mathbb{R}^4 \mid w_B = B_p, \|w - p\| \leq \delta\}.$$

The union

$$\mathcal{D} = \cup_{B_p \in [B_{\text{in}}, B_{\text{out}}]} D_\delta(B_p)$$

forms a four-dimensional compact cylinder. The radius δ is small, but it needs to be at least of $O(\varepsilon)$ to ensure that S^3 lies in \mathcal{D} . The one-parameter family of orbit segments that enter \mathcal{D} via $D_\delta(B_{\text{in}})$ and exit via $D_\delta(B_{\text{out}})$ are candidates for S^3 . To select a unique representative S^3 that S^3 have maximal integration time in \mathcal{D} while satisfying appropriate boundary conditions. Our choice of boundary conditions is explained in section 3.2.

Figure ?? shows a sketch of the unique representative, S^3 in green, in projection onto the (B, A) -plane. Sketched in purple is \mathcal{D} with the spheres $D_\delta(B_{\text{in}})$ and $D_\delta(B_{\text{out}})$ represented as disks at either end; these spheres and \mathcal{D} are for illustration.

3.2. Definition of $W^s(S^3)$ and computation of $W^s(S^3)$ and S^3

We define $W^s(S^3)$ to be a two-parameter family of orbit segments that enter into \mathcal{D} at $D_\delta(B_p)$ for some $B_p \in [B_{\text{in}}, B_{\text{out}}]$, and remain inside \mathcal{D} for $O(1)$ slow time. We select and approximate a specific candidate for $W^s(S^3)$ by requiring that each orbit segment lying on $W^s(S^3)$ have maximal integration time inside \mathcal{D} while satisfying the boundary conditions explained in the following paragraphs. We now turn to the computation of the three-dimensional manifold $W^s(S^3)$ in the same region the two-dimensional stable manifold was investigated in the three-dimensional reduced model considered in [Desroches *et al.*, 2009].

As $W^s(S^3)$ is three dimensional it is challenging to compute and difficult to visualise. Examples of computing and visualising three-dimensional manifolds are in [Waalkens *et al.*, 2005; H\'aro & de la Liave, 2006; Jorba & Olmedo, 2009]. None of these examples are in the context of computing (un)stable manifolds of saddle slow manifolds. Tools to implement the computation of three-dimensional manifolds are not widely

used and, once computed, it is difficult to see the dynamics on the manifold in dimensional projections. Due to the nature of the current computation tools available, computing the entire three-dimensional manifold would also be computationally expensive compared to the the computation of two-dimensional manifolds. A natural way forward is to consider a subset of $W^s(S^3)$ as a one-parameter family of two-dimensional submanifolds. These can be computed by generalizing a method outlined in [Farjami *et al.*, 2018] which can then be implemented in the two-point boundary value problem (2PBVP) continuation package AUTO [Doedel, 2007]. We begin by defining a two-dimensional plane Σ that is transverse to the flow and $\bigcup_{p \in C^3} E^u(p)$ in our region of interest, given by fixed values of A and either X or Y . We approximate a submanifold with a smooth, one-parameter family of solutions to (1) with the property that they begin in Σ , enter \mathcal{D} at $D_\delta(B_p)$ for some $B_p \in [B_{\text{in}}, B_{\text{out}}]$, and remain inside \mathcal{D} for $O(1)$ slow time. We use W_Σ^s to denote the collection of those parts of the orbit segments that enter \mathcal{D} in the fast direction. The later parts that evolve mostly in the B -direction inside \mathcal{D} for $O(1)$ slow time are considered to approximate parts of S^3 . If the later part of the orbit segment includes a fast exit from \mathcal{D} , that fast part is considered as an approximation of an orbit segment lying on the unstable manifold of S^3 , $W^u(S^3)$.

We explain first how to compute a specific submanifold $W_{\widehat{\Sigma}}^s$ for the plane $\widehat{\Sigma}$. The plane $\widehat{\Sigma}$ is defined by the constant values $A \approx 10.6055$ and $Y \approx 0.000230006$. These values are, respectively, the A - and Y -coordinates of the point $p_{\text{out}} \in C^3$ that has a B -coordinate value of $B_{\text{out}} = 0.9$. We then explain how to adjust the computation of $W_{\widehat{\Sigma}}^s$ for the computation of W_Σ^s for a different plane, Σ .

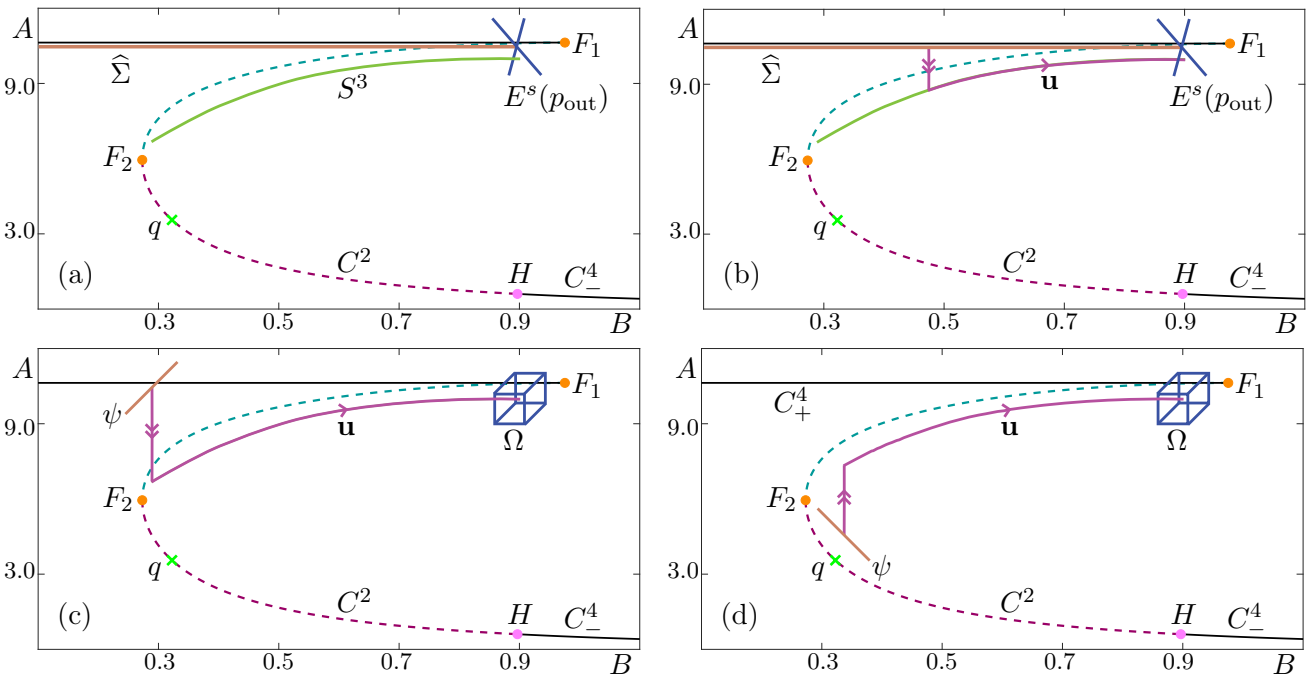


Fig. 3. A sketch of the numerical set-up for the computation of submanifolds of $W^s(S^3)$ in projection onto the (B, A) -plane. Panel (a) shows a sketch at the start of the first homotopy step for computing $W_{\widehat{\Sigma}}^s$ with S^3 (represented by a green curve), $E^s(p_{\text{out}})$ (represented by a blue cross), and the plane $\widehat{\Sigma}$ (represented by a mocha line) which is defined by the A - and Y -coordinates of the point p_{out} . Panel (b) shows a representative orbit segment \mathbf{u} (represented by a magenta curve) of the first homotopy step. Panel (c) shows an illustration of the selection of a \mathbf{u} (represented by a magenta curve) with maximal integration time that starts at ψ (represented by a mocha line) and ends on Ω (represented by a blue cube) which is spanned by $E^s(p_{\text{out}})$ and a vector in the B -direction; the one-dimensional subset $\psi \subset \widehat{\Sigma}$ is defined by fixing $B = B_{\text{in}}$. Panel (d) shows a sketch of the selection of a different submanifold W_Σ^s for Σ on the other side of the critical manifold. Also shown are C^2 , C^3 , C_\pm^4 , F_1 , F_2 , H and q .

We compute the submanifold $W_{\widehat{\Sigma}}^s$ as a one-parameter family of orbit segments $\mathbf{u} = \{\mathbf{u}(s) | 0 \leq s \leq 1\}$ of the rescaled system

$$\frac{d\mathbf{u}}{ds} = TF(\mathbf{u}), \quad (4)$$

where $\mathbf{u}(s) = (A(s), B(s), X(s), Y(s)) \in \mathbb{R}^4$ is the vector of chemical concentrations, F is the right-hand side of (1) and T is the total integration time on the fast timescale, $t = Ts$.

We obtain a first solution on $W_{\widehat{\Sigma}}^s$ via a homotopy step. Following the definition for $W_{\widehat{\Sigma}}^s$, we impose the condition

$$\mathbf{u}(0) \in \widehat{\Sigma} \quad (5)$$

that is, we impose two restrictions on the startpoint of the orbit segment \mathbf{u} , $\mathbf{u}(0)$ because $\widehat{\Sigma}$ is two dimensional. As part of selecting a \mathbf{u} that has a fast approach and remains close to S^3 for $O(1)$ slow time, we consider the two-dimensional eigenspace $E^s(p_{\text{out}}^t)$ that is transverse to $W^u(S^3)$. We define the boundary condition

$$\mathbf{u}(1) \in E^s(p_{\text{out}}^t) \quad (6)$$

that imposes two restrictions on the endpoint of \mathbf{u} , $\mathbf{u}(1)$ and allows for the possibility of $\mathbf{u}(1)$ intersecting $W^u(S^3)$. The point p_{out} is then a solution of the 2PBVP defined by (4), (5) and (6) with $T = 0$. Figure ?? illustrates the set up for this homotopy step in projection onto the (B, A) -plane. Here, the plane $\widehat{\Sigma}$ is projected to a line (mocha), $E^s(p_{\text{out}}^t)$ is represented by a blue cross, and a line representing S^3 is sketched in green. Note that in the (B, A) -projection, $\widehat{\Sigma}$ is directly underneath C_+^4 with respect to the variable A . The saddle equilibrium q is represented as a green x .

We increase the total integration time while allowing the B -coordinate value of $\mathbf{u}(0)$ to decrease towards F_2 . Note that increasing integration time in this fashion causes T to become negative. This step is illustrated in Figure ?? where an intermediate orbit segment is represented as a magenta curve illustrating the presence of a fast segment (double arrows) followed by a slow segment (single arrow). The continuation is stopped at $\mathbf{u}(0)_B = B_{\text{in}} = 0.275$, just before $\mathbf{u}(0)_B$ reaches the B -coordinate value of F_2 . A sketch of the resulting orbit segment is shown in Figure ??.

The orbit segment illustrated in Figure ?? belongs to a two-parameter family of solutions \mathbf{u} of (4) that satisfy the boundary conditions (5) and (6). To select a one-parameter family of orbit segments from these, we select for each $B \in [B_{\text{in}}, B_{\text{out}}]$ the solution \mathbf{u} with maximal integration time such that $\mathbf{u}(0)_B = B$. To find an initial orbit segment satisfying this condition, we define the curve $\psi = \widehat{\Sigma} \cap \{\omega \in \mathbb{R}^4 \mid \omega_B = B_{\text{in}}\}$ and require

$$\mathbf{u}(0) \in \psi, \quad (7)$$

which imposes three conditions on $\mathbf{u}(0)$ and is more restrictive than (5). The boundary condition (7) is represented as a mocha line in Figure ???. We lessen the restrictions on $\mathbf{u}(1)$ and define the three-dimensional space Ω spanned by the two stable eigenvectors of p_{out} and $(0, 1, 0, 0)^{tr}$. Note that Ω is transverse to $\cup_{p \in C^3} E^u(p)$ and, hence, $W^u(S^3)$. Instead of (6) we require

$$\mathbf{u}(1) \in \Omega, \quad (8)$$

which imposes only one condition on $\mathbf{u}(0)$. Condition (8) is represented in Figure ?? as a cube with dark blue edges. We now track the solution \mathbf{u} of the 2PBVP (4), (7), (8) as T becomes more negative, forcing $\mathbf{u}(0)$ to approach $W^s(S^3) \cap \widehat{\Sigma}$ and $\mathbf{u}(1)$ to approach $W^u(S^3) \cap \Omega$. When a fold in T is reached, a (local) minimum in the total integration time T is attained.

The orbit segment that is obtained is not represented in a figure because it is almost identical to the orbit segment illustrated in Figure 3(c): it begins in $\widehat{\Sigma}$ and has a fast approach to S^3 before remaining $O(\varepsilon)$ close for $O(1)$ slow time, and so it lies on $W_{\widehat{\Sigma}}^s$ by definition. In addition to finding an orbit segment

that approximates a solution to (4) laying on $W_{\widehat{\Sigma}}^s$, we can approximate S^3 by restricting the orbit segment further inside $[B_{\text{in}}, B_{\text{out}}]$ to exclude fast segments. At this stage the entire solution family lying on $W_{\widehat{\Sigma}}^s$ can be computed by continuing the fold in T , while allowing $u(0)_B$ to increase.

Figure 4 shows two projections of $W_{\widehat{\Sigma}}^s$. Although the manifold is two dimensional, it is necessary to visualise it in both (B, A, X) - and (B, A, Y) -projections because it exists in four-dimensional space. Lying on $W_{\widehat{\Sigma}}^s$ is a representative orbit segment, plotted in magenta. The critical manifold is plotted and the view is rotated relative to earlier figures to help illustrate the geometry of the submanifold. Orbits lying on $W_{\widehat{\Sigma}}^s$ have a fast approach to S^3 in X and Y before approaching mainly in the A -direction and then finally remaining close to C^3 for $O(1)$ slow time.

In the case where we would like to compute W_{Σ}^s where Σ is defined by different constant values of A and Y (or X), we can obtain a first orbit segment on $W_{\widehat{\Sigma}}^s$ via a second homotopy step. Using an intermediate orbit segment from the first homotopy step as a starting point, we impose (6) while keeping as free parameters T , $u(0)_B$, and the X -coordinate $u(0)_X$ of $u(0)$ (or the Y -coordinate $u(0)_Y$ of $u(0)$). In two runs, we continue u with $u(0)_A$ and $u(0)_Y$ (or $u(0)_X$) as main continuation parameters. In each of these runs, we increase or decrease the main continuation parameter until it attains the value necessary for $u(0) \in \Sigma$. Once $u(0) \in \Sigma$, we follow the rest of the procedure described above while considering Σ instead of $\widehat{\Sigma}$.

Figure ?? illustrates a choice of Σ on the opposite side of the critical manifold from $\widehat{\Sigma}$ with respect to the A -coordinate in the (B, A) -projection. The orbit segment resulting from the second homotopy step is represented as a magenta curve. Conditions (7) and (8) are again illustrated with a mocha line and a cube with dark blue edges, respectively.

Figure 5 shows $W_{\widehat{\Sigma}}^s$ together with one other submanifold W_{Σ}^s of $W^s(S^3)$. The additional submanifold was selected with Σ given by $A = 2.0$ and $Y = 0.0$. Figure 6 shows the two submanifolds of W^s shown in Figure 5 along with three additional submanifolds and the planes Σ that define them. The additional submanifolds were selected with Σ given by $A = 4.0$ and $X = 0.75$, $A = 4.0$ and $Y = 0.75$, and $A = 6.0$ and $X = 0.5$. Note that the Σ appear as lines in one of the two projections, depending on whether they are defined by constant values of X or Y . The submanifolds appear to intersect, however this is due to the variable A being slower than variables X and Y . This causes orbit segments to approach S^3 in the X - and Y -directions before approaching in the A -direction and is the reason for the portions of the submanifolds that come very near to each other.

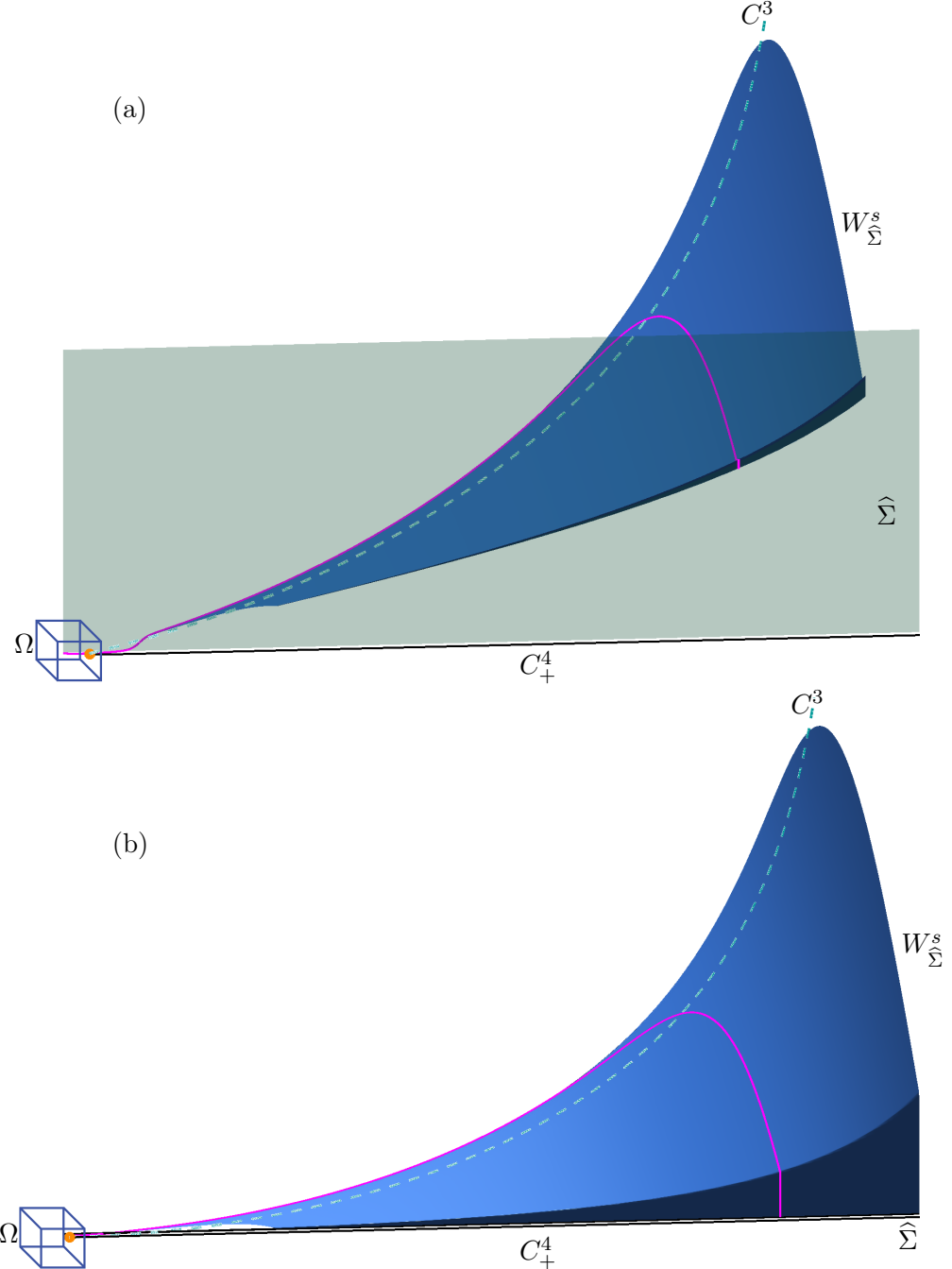


Fig. 4. The submanifold $W_{\widehat{\Sigma}}^s$ (light blue surface) of $W^s(S^3)$ shown in projection onto (B, A, X) -space (a) and onto (B, A, Y) -space (b) with a representative orbit segment (magenta curve), $\widehat{\Sigma}$ (mint surface and line), and Ω (represented by a blue cube). Also shown are C^3 , C_+^4 , and F_1 . The view is rotated relative to previous figures.

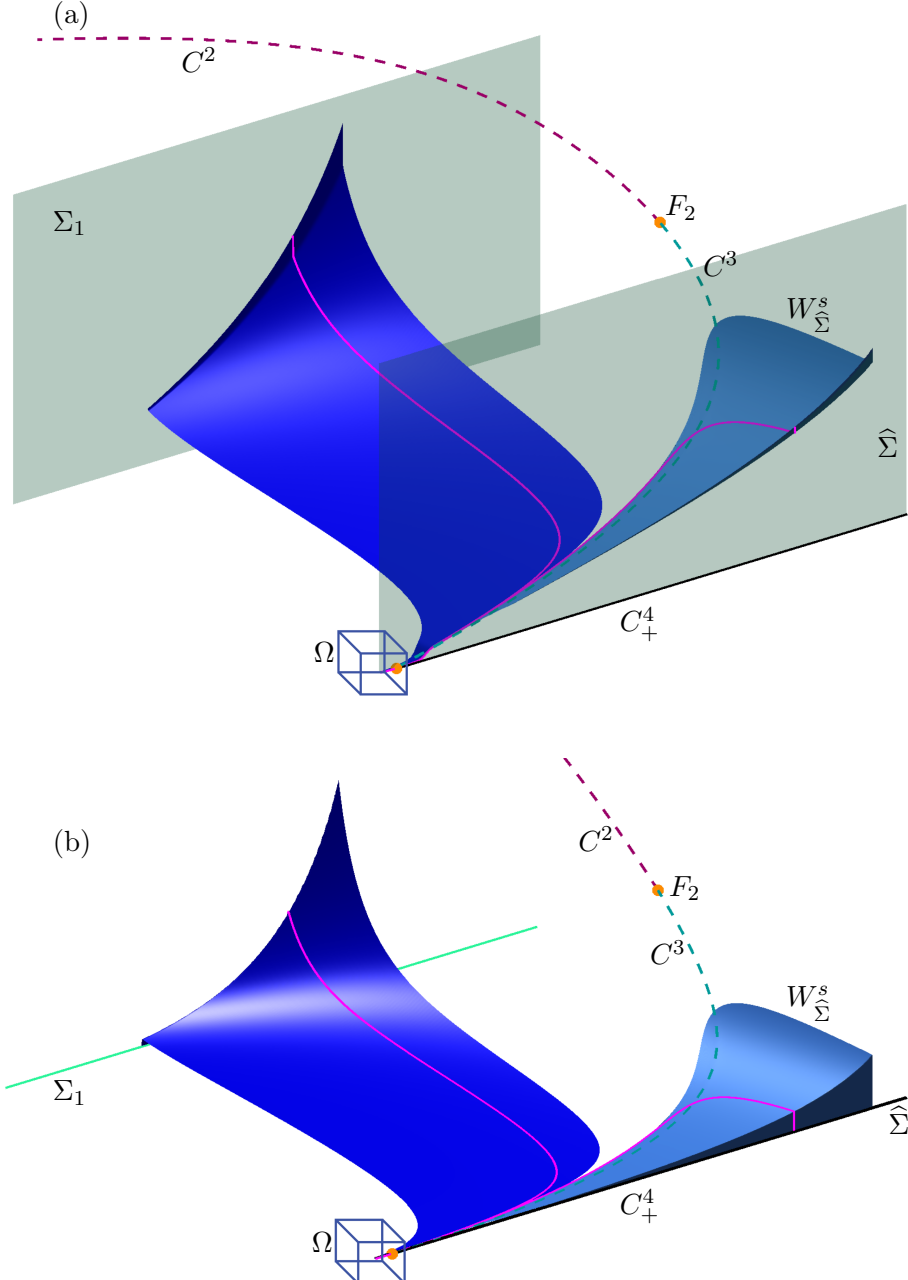


Fig. 5. The submanifolds $W_{\Sigma_1}^s$ (blue surface) and $W_{\widehat{\Sigma}}^s$ (light blue surface) of $W^s(S^3)$ shown in projection onto (B, A, X) -space (a) and onto (B, A, Y) -space (b) with representative orbit segments (magenta curves), planes $\widehat{\Sigma}$ (mint surface and line) and Σ_1 (mint surface and line), and Ω (represented by a blue cube). Also shown are C^2 , C^3 , C_+^4 , F_1 , and F_2 .

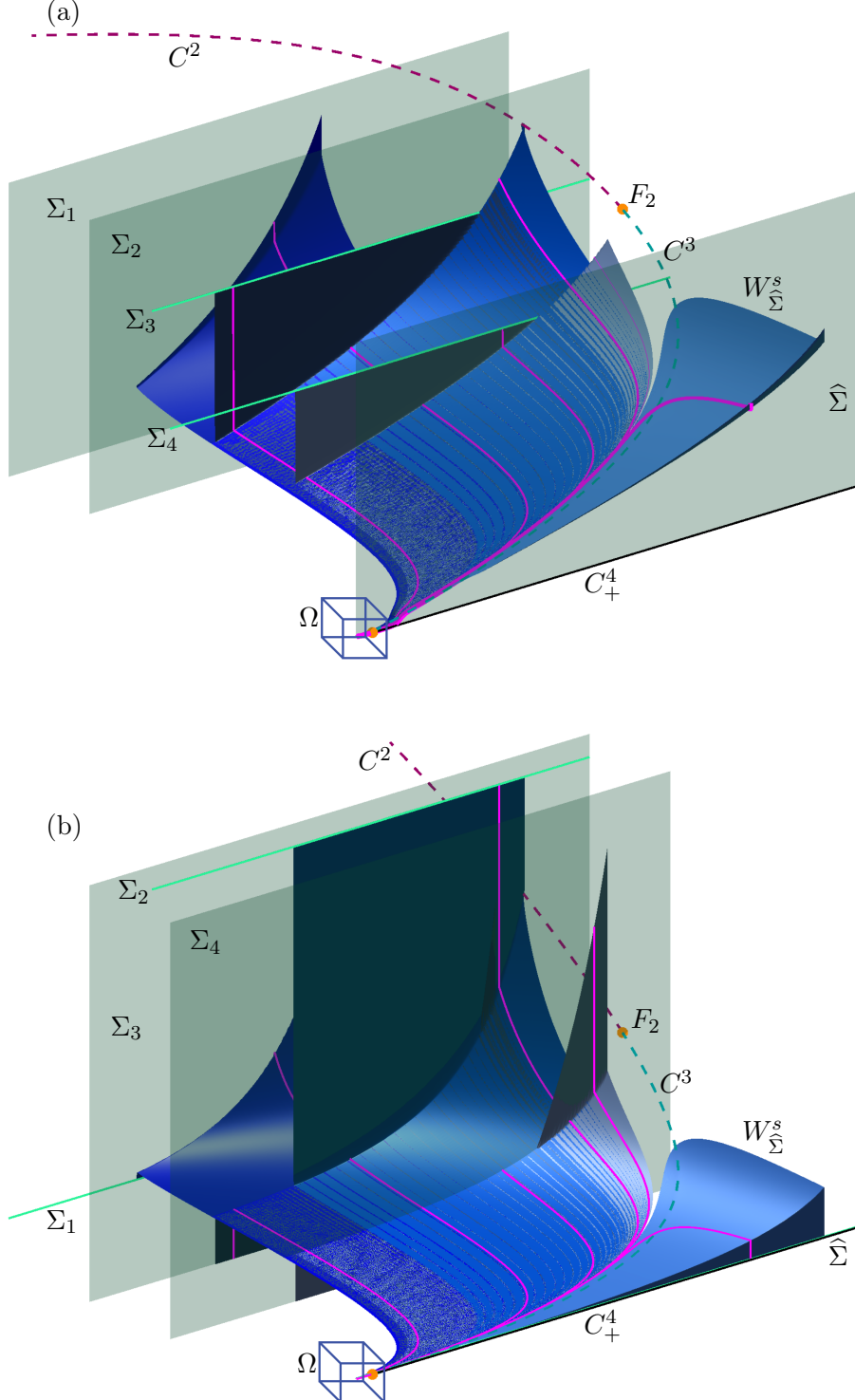


Fig. 6. The submanifolds from Figure 5. with three additional submanifolds $W_{\Sigma_i}^s$ (blue surfaces) defined by Σ_2 , Σ_3 , and Σ_4 (magenta planes and lines) shown in projection onto (B, A, X) -space (a) and onto (B, A, Y) -space (b) with Ω (represented by a blue cube). An example orbit segment (magenta curve) is plotted on each $W_{\Sigma_i}^s$. Also shown are C^2 , C^3 , C_+^4 , F_1 , and F_2 .

We note that, unlike the stable manifold of S^3 computed for the reduced system in [Desroches *et al.*, 2009], each submanifold W_{Σ}^s in Figure 6 diverges backwards in time in the X - and Y -directions before reaching S^2 . The computations in [Desroches *et al.*, 2009] suggest that there exists a submanifold of $W^s(S^3)$ in the four-dimensional system that spirals around S^2 in backward time for an appropriate choice of Σ .

Such a surface would be the intersection of the two three-dimensional manifolds $W^s(S^3)$ and $W^u(S^2)$ in the full four-dimensional system.

Stuff to add into text: Here Σ_1 is given by $A = 2.0$ and $Y = 0.0$. Here, Σ_2 is given by $A = 4.0$ and $Y = 0.75$, Σ_3 by $A = 4.0$ and $X = 0.75$, and Σ_4 by $A = 6.0$ and $X = 0.5$.

3.3. Definition and computation of $W^u(S^2)$

Before investigating the existence of such an intersection, we first consider the unstable manifold $W^u(S^2)$ of S^2 . The computation of submanifolds of $W^u(S^2)$ is similar to the computation of W_Σ^s , however adjustments must be made in light of some complicating challenges. Two extra challenges are the saddle equilibrium, q , of the full system lying on C^2 at $B = 0.323$ and the Hopf bifurcation of the fast subsystem at $B = 0.897$. Additional care must be taken to ensure that the computed orbits do not increase in integration time solely by approaching the saddle equilibrium's stable manifold or by following the nearby stable slow manifold backward in time. Values for B_{in} and B_{out} are chosen such that $q_B < B_{\text{out}} < B_{\text{in}} < H_B$. We can then define the four-dimensional cylinder \mathcal{D} similarly to how it was defined for $W^s(S^3)$. The unstable manifold can then be defined as a two-parameter family of orbit segments composed of a collection of one-parameter families that enter \mathcal{D} at B_{in} , follow S^2 for an $O(1)$ amount of slow time and then exit at B_p for each $B_p \in [B_{\text{in}}, B_{\text{out}}]$. We modify the steps for computing two-dimensional submanifolds of $W^s(S^3)$ in order to ensure that an increase in integration time results only from a more accurate approximation of a submanifold of $W^u(S^2)$.

Namely, we must make adjustments to boundary conditions so that orbit segments do not increase in integration time by approaching q or by following the attracting slow manifold to the right of the Hopf bifurcation in the (B, A) -projection in backwards time. To compute a submanifold of $W^u(S^2)$, we define for each $B_p \in [B_{\text{in}}, B_{\text{out}}]$ a sphere in the subspace $\{B = B_p\}$, centered at p and with radius r ; here $p \in C^2$ is the unique point such that $p_B = B_p$. More formally,

$$\tilde{D}_r(B_p) = \{w \in \mathbb{R}^4 \mid w_B = B_p, \|w - p\| = r\}.$$

We can then define the three-dimensional cylinder $\mathcal{R} = \cup_{B \in [B_{\text{in}}, B_{\text{out}}]} \tilde{D}_r(B)$.

We define a submanifold W_r^u for $r > \delta$, as the one-parameter family of orbit segments that enter \mathcal{D} at B_{in} and, for each $B_p \in [B_{\text{in}}, B_{\text{out}}]$, intersect \mathcal{R} after exiting \mathcal{D} at B_p an $O(1)$ amount of slow time afterwards. The radius δ is chosen small enough so that \mathcal{R} does not contain a locus of points at which the flow is not transverse to \mathcal{R} . We use the cylinder \mathcal{R} instead of the plane Σ described in section 4.1 to keep the endpoints of orbit segments \mathbf{u} close enough to C^2 so that the \mathbf{u} cannot contain segments that approach q . In the following steps, the computation of a submanifold $W_{r^*}^u$ is outlined for $r^* = 0.7$ before the description of the necessary modifications to obtain W_r^u for more general r .

We perform an initial homotopy step analogous to the homotopy step in section 4.1 to obtain an orbit segment that enters \mathcal{D} at B_{in} and intersects \mathcal{R} after exiting \mathcal{D} at some $B^* \in [B_{\text{in}}, B_{\text{out}}]$. We select the unique point $\bar{p} \in C^2$ such that $\bar{p}_B = 0.7$. The plane $\bar{\Sigma}$ is defined by fixing the A - and Y - coordinates of \bar{p} , which are $A \approx 0.940272$ and $Y \approx 1.342954$. We impose the boundary conditions

$$\mathbf{u}(0) \in E^u(\bar{p}), \tag{9}$$

and

$$\mathbf{u}(1) \in \bar{\Sigma} \tag{10}$$

which each impose two conditions on $\mathbf{u}(0)$ and $\mathbf{u}(1)$, respectively. The point \bar{p} is then a solution to the 2PBVP defined by (4), (9), and (10) for $T = 0$. We increase T while $\mathbf{u}(1)_B$ decreases and stop the continuation when $\mathbf{u}(1)$ intersects \mathcal{R} . This step is almost identical to the initial homotopy step in section 4.1 except that we reverse the direction of time and instead of stopping the continuation when $\mathbf{u}(1)_B$ attains a certain value, we stop the continuation when $\mathbf{u}(1)$ intersects \mathcal{R} . We denote by B_{stop} the B -value of $\mathbf{u}(1)$ at the end of this step and p^{stop} the corresponding point in C^2 .

We perform a second homotopy step to ensure that $\mathbf{u}(0)$ is such that \mathbf{u} can approach S^2 for $O(1)$ slow time while also ensuring that \mathbf{u} doesn't increase in integration time by following the attracting slow manifold for longer backward time. In the second homotopy step we define a three-dimensional space $\Xi_{\text{HOM2}} = E^u(\bar{p}) + \text{span}\{(0 \ B \ 0 \ 0)^{\text{tr}}\}$ and a one-dimensional circle $\Theta = \{w \in \mathbb{R}^4 \mid w_Y = \bar{p}_Y, w_B = B_{\text{stop}}, \|w - p^{\text{stop}}\| = 0.7\}$. Then the orbit segment resulting from the first homotopy step is a solution to the 2PBVP defined by (4),

$$\mathbf{u}(0) \in \Xi_{\text{HOM2}}, \quad (11)$$

and

$$\mathbf{u}(1) \in \Theta. \quad (12)$$

Our goal is to continue the orbit segment by increasing T such that $u(0)_B$ increases, that is (11) drives the continuation. Condition (12) is chosen such that integration time does not increase with decreasing $\mathbf{u}(1)_B$ and so that our 2PBVP is well defined. The continuation is stopped when $\mathbf{u}(0)_B = 1.0$. The resulting orbit segment is initially attracted to the attracting slow manifold and follows it until it passes near \mathcal{H} at which point \mathbf{u} follows S^2 . As following the attracting slow manifold for longer backwards time requires the increase of $\mathbf{u}(0)_B$, we fix $\mathbf{u}(1)_B$ from this step onwards to ensure that this does not occur. This is different from section 4.1 in which $\mathbf{u}(1)_B$ remained unfixed in the final steps of the computation.

To fix $\mathbf{u}(0)_B$, we define the plane $\Phi = \{w \in \Xi_{\text{HOM2}} \mid w_B = 1.0\}$ and impose the boundary conditions

$$\mathbf{u}(0) \in \Phi, \quad (13)$$

and

$$\mathbf{u}(1) \in \{w \in \mathcal{R} \mid w_B = B_{\text{stop}}\}. \quad (14)$$

Condition (14) requires that $\mathbf{u}(1)$ remain on a two-dimensional sphere as opposed to the one-dimensional curve ψ described for condition (7) in section 4.1. We must allow this extra degree of freedom for $\mathbf{u}(1)$ as keeping $\mathbf{u}(0)_B$ fixed in condition (13) imposes an extra constraint compared to condition (8) in section 4.1. Our aim is to select a smooth one-parameter family of orbit segments from the two-parameter family of orbit segments satisfying the 2PBVP defined by (4), (13), and (14) to which the orbit segment resulting from the second homotopy step is a solution. To this end, for each $B_p \in [B_{\text{in}}, B_{\text{out}}]$, we select from the one-parameter family of orbit segments exiting \mathcal{D} at B_p the orbit segment with maximal integration time. To find an initial orbit of this description we increase T again until maximal integration time is reached. This is detected as a fold in T . Finally to obtain the rest of the submanifold $W_{r^*}^u$ we switch the endpoint boundary condition to

$$\mathbf{u}(1) \in \mathcal{R} \quad (15)$$

which imposes one condition on $\mathbf{u}(1)$. In two runs, the fold in T is continued until $\mathbf{u}(0)_B = B_{\text{out}} = 0.35$ and then again until $\mathbf{u}(0)_B = B_{\text{in}} = H_B$ to sweep out $W_{r^*}^u$.

Figure 7 shows two projections of the submanifold $W_{r^*}^u$. Example orbit segments lying on $W_{r^*}^u$ are plotted in forest green and a subset of C^2 is plotted in raspberry. The view is rotated relative to previous figures.

We can compute a different submanifold W_r^u by returning to the second homotopy step in our computation. Depending on the magnitude of r , we may need to perform one or two additional homotopy steps. In the case where r is large enough that $\tilde{D}_r(\mathbf{u}(1)_B)$ contains a locus of points at which the flow is not transverse to it, an extra homotopy step is needed. We define a plane Ξ_{hom3} by fixing the A - and X -coordinates of $\mathbf{u}(1)$ after the second homotopy step. To ensure that our 2PBVP is well defined, the orbit segment is continued with the boundary conditions (13) and

$$\mathbf{u}(1) \in \Xi_{\text{hom}3}, \quad (16)$$

which imposes two conditions on $\mathbf{u}(1)$. The endpoint B -coordinate $\mathbf{u}(1)_B$ is increased until $\tilde{D}_r(\mathbf{u}(1)_B)$ no longer contains a locus of tangent points.

The final homotopy step involves defining another plane Ξ_{homfinal} by fixing the B - and X - values of $\mathbf{u}(1)$. Condition (13) is imposed while a new restriction

$$\mathbf{u}(1) \in \Xi_{\text{homfinal}}, \quad (17)$$

imposes two conditions on $\mathbf{u}(1)$. The radius r is then increased or decreased until the desired magnitude is attained. All that remains is to follow through with the rest of the steps to compute W_r^u . In the last step, B_{out} is chosen such that the flow is transverse to $\tilde{D}(B_{\text{out}})$. We do not show several submanifolds of $W^u(S^2)$ in the same figure, because the spiralling dynamics near C^2 make visualisation difficult in the (B, A, X) - and (B, A, Y) -projections due to (self)-intersections of the submanifolds in these projections.

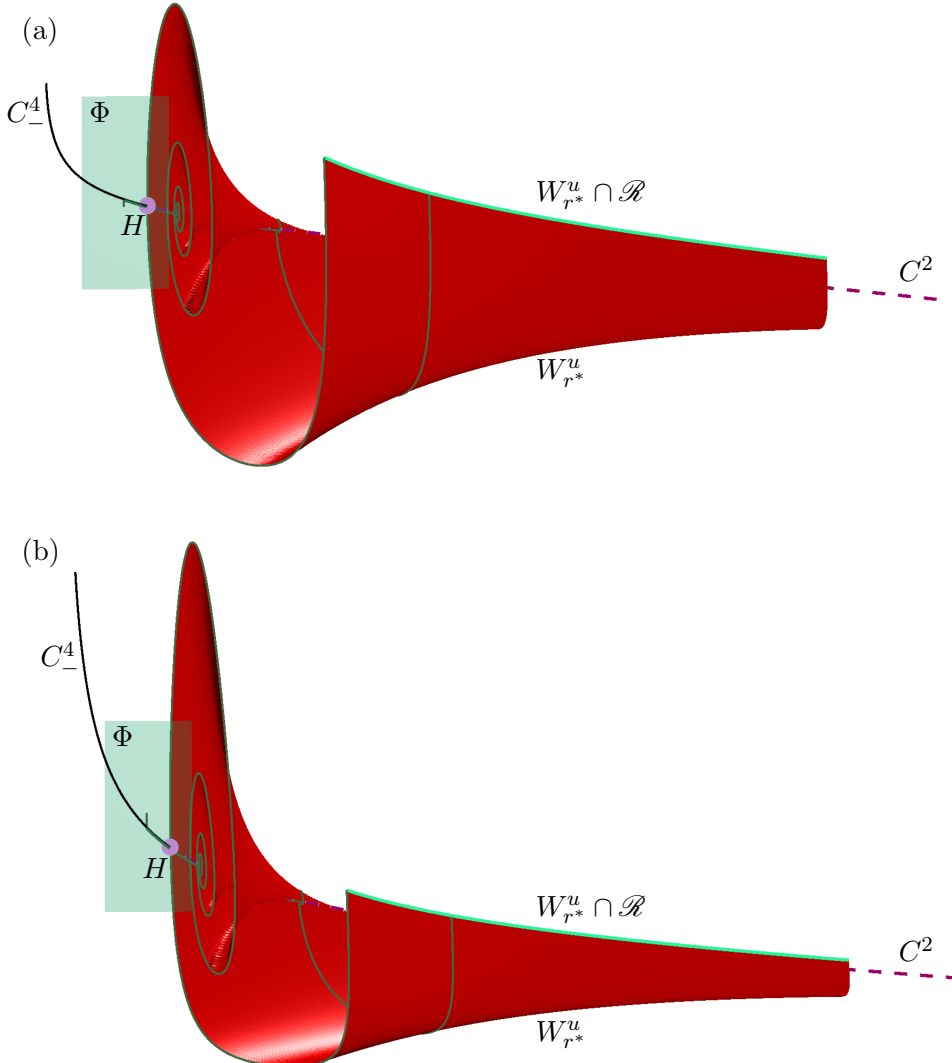


Fig. 7. The submanifold W_r^u (red surface) of $W^u(S^2)$ shown in projection onto (B, A, X) -space (a) and (B, A, Y) -space (b); also shown are two representative orbit segments (forest green curves) on W_r^u , Φ (mint surface), and the intersection $W_r^s \cap \mathcal{R}$ (mint curve). Branches C^2 and C^4 are also shown and the view is rotated relative to previous figures. Also shown are C^2 , C^4 , and H .

4. A heteroclinic connection between two saddle slow manifolds

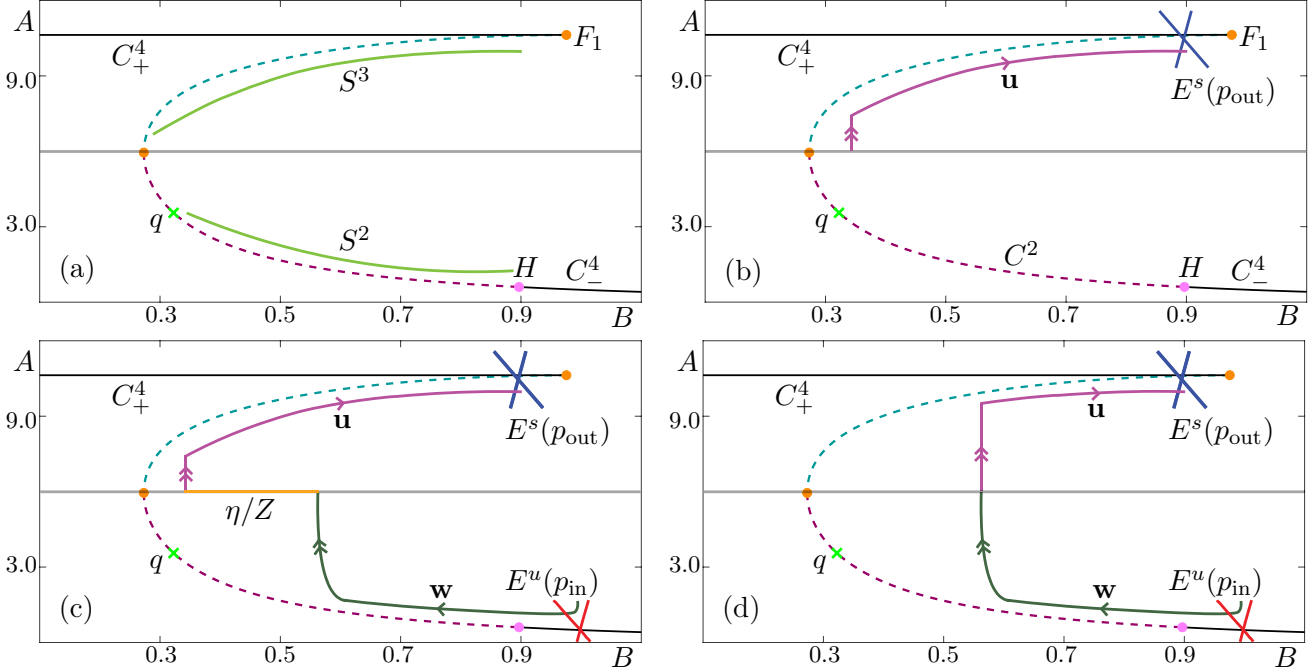


Fig. 8. Numerical set up for the computation of \mathcal{H} with Lin's method. Panel (a) shows the critical manifold with S^3 and S^2 sketched in green. The Lin section \mathcal{L} is sketched in charcoal. Panel (b) shows an initial orbit segment \mathbf{u} laying on $W^s(S^3)$ such that $\mathbf{u}(0) \in \mathcal{L}$. Also shown in (b) is $E^s(p_{\text{out}})$ for \mathbf{u} is sketched as a blue cross. Panel (c) additionally shows a sketch of an initial orbit segment \mathbf{w} on $W^u(S^2)$ such that $\mathbf{w}(1) \in \mathcal{L}$. The unstable eigenspace $E^u(p_{\text{in}})$ for \mathbf{w} is sketched as a red cross. The Lin vector Z , connecting $\mathbf{u}(0)$ and $\mathbf{w}(1)$ inside \mathcal{L} , is sketched in gold on top of the sketch of \mathcal{L} . Panel (d) shows \mathbf{u} and \mathbf{w} after the Lin gap η is closed and $\mathbf{u}(0) = \mathbf{w}(1) \in \mathcal{L}$.

The two three-dimensional manifolds $W^s(S^3)$ and $W^u(S^2)$ are likely to intersect generically in a two-dimensional manifold of heteroclinic connections in the four-dimensional phase space. We denote the surface of intersections \mathcal{H} . We can compute such a surface of connections with an approach known as Lin's method [Lin, 1989; Krauskopf & Rieß, 2008; Zhang *et al.*, 2012]. Since Lin's method is typically used in parameter continuation of heteroclinic connections that are not structurally stable, we explain the set-up here for our context. We first choose a three-dimensional so-called Lin section \mathcal{L} that divides the four-dimensional phase space into two regions such that S^3 lies in one region and S^2 is in the other. We then compute an orbit segment \mathbf{u} lying on $W^s(S^3)$ and continue it in several homotopy steps until $\mathbf{u}(0) \in \mathcal{L}$. We also compute an orbit segment \mathbf{w} on $W^u(S^2)$ and continue it until $\mathbf{w}(1) \in \mathcal{L}$ as well.

We define a vector $\mathbf{v}_Z \in \mathbb{R}^4$ called a Lin vector and given by

$$\mathbf{v}_Z = \frac{\mathbf{u}(0) - \mathbf{w}(1)}{\|\mathbf{u}(0) - \mathbf{w}(1)\|} \quad (18)$$

as well as two unit normal vectors $\mathbf{n}_1, \mathbf{n}_2 \in \mathcal{L}$ such that $\mathbf{n}_i \perp \mathbf{v}_Z$ for $i = 1, 2$ and $\mathbf{n}_1 \perp \mathbf{n}_2$. While our choice for the vector \mathbf{v}_Z , and normal vectors \mathbf{n}_1 and \mathbf{n}_2 is arbitrary, their selection remains fixed for the remainder of the computation. The span of \mathbf{v}_Z defines a one-dimensional space, $Z \subset \mathcal{L}$, called a Lin space. The distance between $\mathbf{u}(0)$ and $\mathbf{w}(1)$ in Z defines the a Lin gap which is a regular test function which we denote η . We approximate an orbit segment on \mathcal{H} by continuation in the direction of decreasing η while requiring $\mathbf{u}(0), \mathbf{w}(1) \in Z$. When $\eta = 0$, an orbit segment on \mathcal{H} is detected as the concatenation of \mathbf{w} and \mathbf{u} at this continuation step.

In our computations of \mathbf{u} and \mathbf{w} we do not find the orbit segments with maximal integration time as it is not straightforward to track two folds simultaneously with the automatic fold continuation in the

package AUTO [Doedel, 2007]. A discussion of the numerical accuracy of our results follows in the next section. Since we are not requiring that \mathbf{w} satisfy the condition of maximal integration time, we do not run into the same issues encountered in section 4.2 for the computation of a submanifold of $W^u(S^2)$. For this reason we may compute \mathbf{w} without considering the distance of $\mathbf{w}(1)$ from C^2 .

4.1. Computing an initial orbit segment on $W^s(S^3)$

The Lin section \mathcal{L} is a three-dimensional section given by a constant A -coordinate. We choose $\mathcal{L} = \{\omega \in \mathbb{R}^4 \mid \omega_A = 6.0\}$ so that, in the (B, A) -projection and with respect to the variable A , it lies between q and the point on C^3 with the same B -coordinate as q . Our choice of \mathcal{L} allows us to avoid stopping the continuation because \mathcal{L} has intersected C^2 . We can instead compute the largest possible portion of \mathcal{H} by continuing orbit segments as close as possible to q . Although \mathcal{L} is three dimensional, it is illustrated as a purple line in the (B, A) -projection in Figure ??.

We compute the orbit segment \mathbf{u} as in the computation of an initial orbit segment on a submanifold W_Σ^s in section 3.2 with the exception that we omit last the step and do not compute the orbit with maximal integration time. Here, Σ is the plane given by $A = 6.0$ and $Y \approx 1.342954$.

4.2. Computing an initial orbit segment on $W^u(S^2)$

We perform three homotopy steps to obtain an initial orbit segment on $W^u(S^2)$. We begin with the point \bar{p} that is a solution to the 2PBVP defined by (4), (9), and (10) for $T = 0$. We obtain an orbit segment \mathbf{w} by imposing conditions (9) and (10) while increasing integration time. The continuation is stopped when $\mathbf{w}(1)_B = 0.6$.

We then impose (11) and (10) while additionally requiring $\mathbf{w}(1)_B = 0.6$. We continue \mathbf{w} while increasing integration time once more while $\mathbf{w}(0)_B$ increases, and stop the continuation when $\mathbf{w}(0)_B = 0.96$.

In the third homotopy step, we impose (13) while keeping $\mathbf{w}(0)_B$, $\mathbf{w}(1)_B$ and $\mathbf{w}(1)_Y$ fixed. The A -coordinate of $\mathbf{w}(1)$ increases as T is increased. The continuation is stopped when $\mathbf{w}(1)_A = 6.0$. In other words, we stop the continuation when $\mathbf{w}(1) \in \mathcal{L}$.

4.3. Closing the Lin gap

We are now in a position to define vectors \mathbf{v}_Z , \mathbf{n}_1 , and \mathbf{n}_2 . We define \mathbf{v}_Z using the orbit segments \mathbf{u} and \mathbf{w} obtained in sections 5.1 and 5.2 and take $\mathbf{n}_1 = (0, 0, \mathbf{v}_{ZY}, -\mathbf{v}_{ZX})^{tr}$, and $\mathbf{n}_2 = (0, \mathbf{v}_{ZY}, 0, -\mathbf{v}_{ZB})^{tr}$. We impose conditions

$$\begin{aligned} \mathbf{u}(0), \mathbf{w}(1) &\in \mathcal{L}, \\ [\mathbf{u}(0) - \mathbf{w}(1)] \cdot \mathbf{n}_1 &= 0, \\ [\mathbf{u}(0) - \mathbf{w}(1)] \cdot \mathbf{n}_2 &= 0 \end{aligned} \tag{19}$$

to restrict $[\mathbf{u}(0) - \mathbf{w}(1)] \in Z$. Additionally, we impose conditions (6) and (13) while allowing the integration times of \mathbf{u} and \mathbf{w} to move freely. The pair of orbit segments \mathbf{u} and \mathbf{w} obtained at the end of section 5.2 are one of a two-parameter family of orbit-segment pairs satisfying (6), (13), and (19). To formulate a well-defined 2PBVP, we impose the restriction

$$\mathbf{w}(1)_B \in \{\omega \in \mathbb{R}^4 \mid \omega_B = 0.6\}, \tag{20}$$

and continue \mathbf{u} and \mathbf{w} while η is decreased. We stop the continuation as soon as $\eta = 0$, at which point the concatenation of \mathbf{w} with \mathbf{u} forms an approximation of a heteroclinic connection in \mathcal{H} .

To obtain a one-parameter family of concatenations approximating \mathcal{H} , we require $\eta = 0$ while relaxing condition (20). We then decrease $\mathbf{w}(1)_B$ and stop the continuation before \mathbf{u} and \mathbf{w} reach the intersection of \mathcal{H} with $W^u(q)$. We sweep out the other side of the manifold by continuation in the opposite direction (of increasing $\mathbf{w}(1)_B$) and stop just before $\mathbf{w}(1)_B$ reaches the B -coordinate of the Hopf bifurcation point H on C^2 .

Figure 14 shows \mathcal{H} projected into (B, A, X) - and (B, A, Y) -space. The portion of \mathcal{H} composed of the collection of orbit segments \mathbf{w} is colored in red and the portion composed of orbit segments \mathbf{u} is blue. Orbit segments on \mathcal{H} spiral around S^2 for an $O(1)$ amount of slow time before exiting via $W^u(S^2)$ and following S^3 for an $O(1)$ amount of slow time via $W^s(S^3)$. Three representative orbit segments are shown, their \mathbf{w} segments in magenta and their \mathbf{u} segments in forest green.

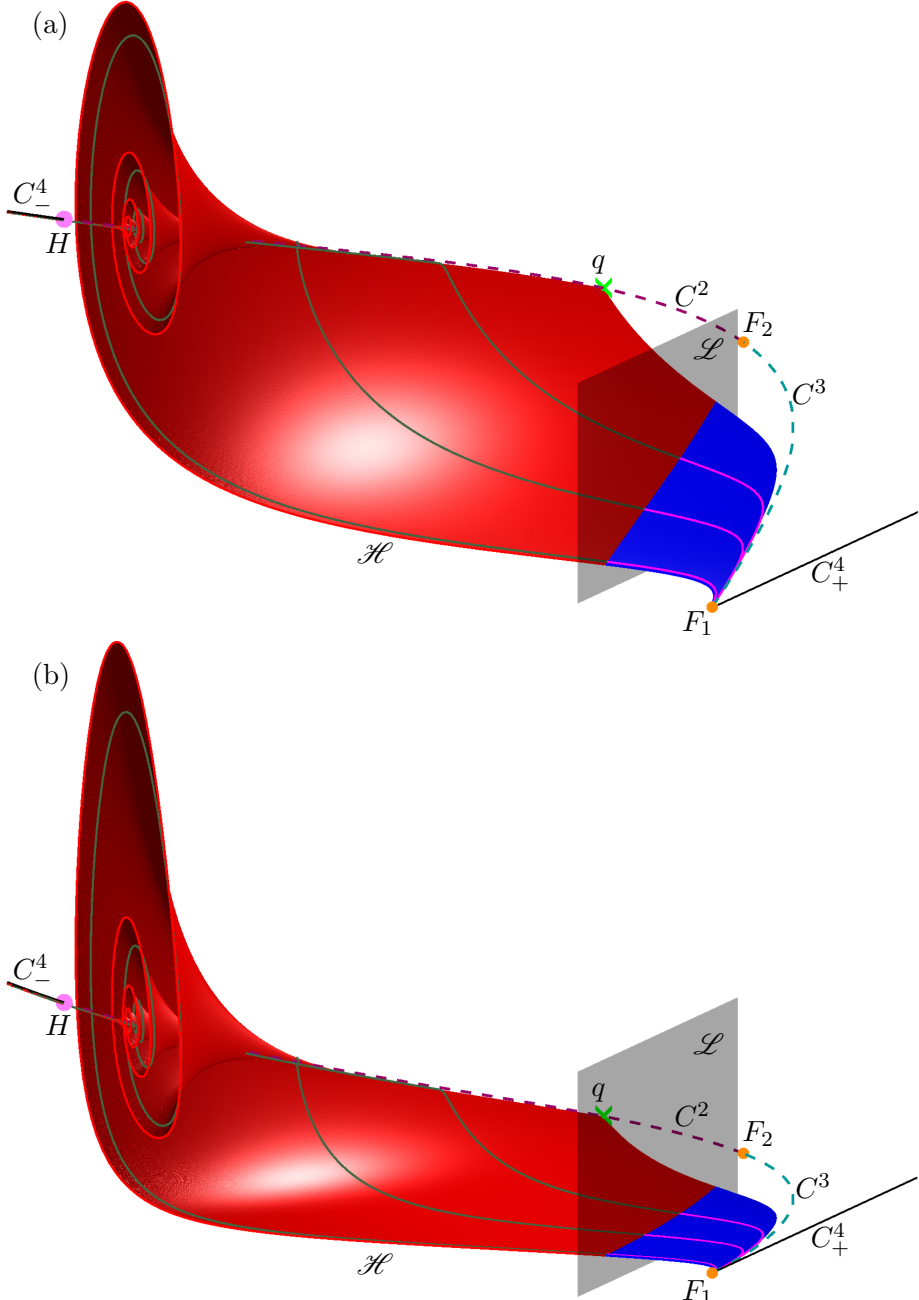


Fig. 9. The surface of heteroclinic connections \mathcal{H} , \mathcal{L} , and the critical manifold projected into (a) (B, A, X) - and (b) (B, A, Y) -space. The portion of \mathcal{H} that was computed as orbit segments in $W^s(S^3)$ is plotted in blue while the portion that was computed as orbit segments laying on $W^u(S^2)$ is plotted in red. Three representative orbit segments laying on \mathcal{H} are plotted. The portions of the orbit segments computed as \mathbf{u} are plotted in magenta while the segments that were computed as \mathbf{w} are plotted in forest green. The three-dimensional Lin section \mathcal{L} is plotted as a charcoal plane in each projection. The saddle equilibrium q is plotted as a green cross, partially obstructed by \mathcal{H} and \mathcal{L} .

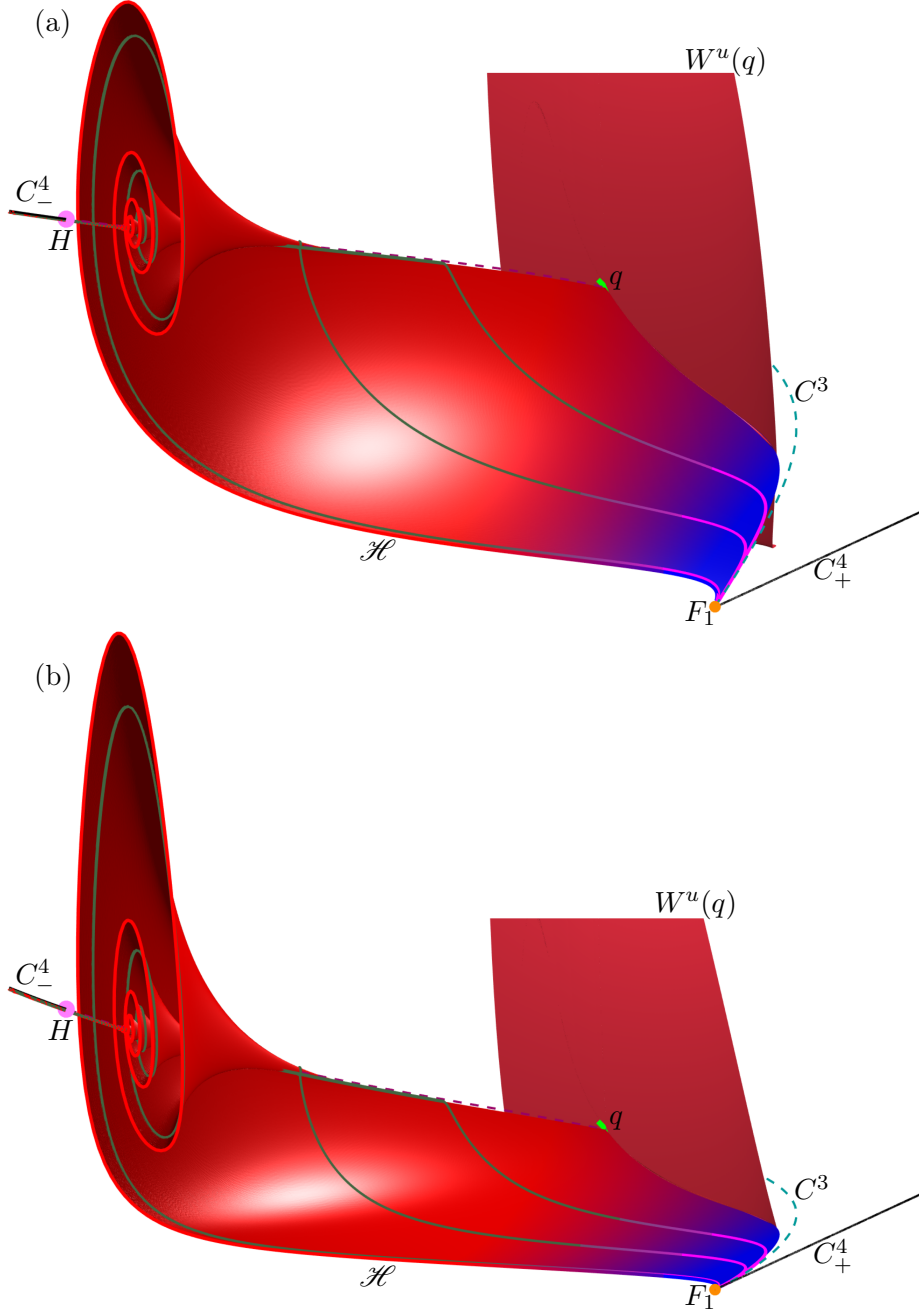


Fig. 10. The surface of heteroclinic connections \mathcal{H} (red-blue fade) shown with $W^u(q)$ (burgundy) and the critical manifold projected into (a) (B, A, X) - and (b) (B, A, Y) -space. The saddle equilibrium q (green cross) is partially obstructed by \mathcal{H} and $W^u(q)$.

5. Computing the singular surface of heteroclinic connections

The computation of the surface of heteroclinic connections, \mathcal{H}_0 , for $\varepsilon = 0$ is slightly different from the computation of \mathcal{H} for $\varepsilon > 0$. The time scaling parameter, ε , being zero means that $\mathcal{H}_0 = W^s(C^3) \cap W^u(C^2)$. The surface \mathcal{H}_0 is then composed of the family of heteroclinic connections in (2) parameterized by B . In the (B, A) -projection on C^2 , the equilibria to the left of $B \approx 0.476858$ have all real eigenvectors and equilibria to the right have a complex conjugate pair of eigenvectors. Due to the change in the type of eigenvectors, two slightly different algorithms are used to compute \mathcal{H} in two pieces. We first describe the computation for equilibria with real eigenvectors and then for equilibria with complex conjugate eigenvectors.

For both computations, we consider solutions to the rescaled system

$$\frac{d\mathbf{u}}{ds} = TG(\mathbf{u}), \quad (21)$$

where $\mathbf{u}(s) = (A(s), X(s), Y(s)) \in \mathbb{R}^3$ is the vector of chemical concentrations, G is the right hand side of (2), and T is integration time on the fast timescale $t = Ts$. The Lin section \mathcal{L} is again taken to be the space defined by a constant $A = 6.0$. Note that in the layer equation, \mathcal{L} is two dimensional and B is a parameter.

5.1. Real eigenvalues

For the first three steps of the computation, the parameter B is kept constant at a value of 0.4. We compute an initial orbit segment on $W^s(C^3)$ following the algorithm for computing a two-dimensional global manifold as a solution family of BVPs outlined in [Krauskopf *et al.*, 2007]. We consider the equilibrium $\tilde{p}_{\mathfrak{R}}$ of (2) for $B = 0.4$ such that $(\tilde{p}_{\mathfrak{R}_A}, 0.4, \tilde{p}_{\mathfrak{R}_X}, \tilde{p}_{\mathfrak{R}_Y}) \in C^3$. We define a plane $\tilde{\Sigma}_{\mathfrak{R}} = \{\omega \in \mathbb{R}^3 \mid \omega_Y = \tilde{p}_{\mathfrak{R}_Y}\}$ and a one-dimensional circle $\tilde{\Gamma}_{\mathfrak{R}} = \{\omega \in \mathbb{R}^3 \mid \tilde{p}_{\mathfrak{R}} + r_{\mathfrak{R}}(\mathbf{v}_1 \sin(\theta) + \mathbf{v}_2 \cos(\theta)), \theta \in [0, 2\pi)\}$ where $r_{\mathfrak{R}} = 0.0001$ and \mathbf{v}_1 and \mathbf{v}_2 are the stable eigenvectors of $\tilde{p}_{\mathfrak{R}}$. The radius $r_{\mathfrak{R}}$ of $\tilde{\Gamma}_{\mathfrak{R}}$ is chosen small enough that $\tilde{\Gamma}_{\mathfrak{R}}$ approximates a curve lying on $W^s(\tilde{p}_{\mathfrak{R}})$ and large enough that AUTO can distinguish points on $\tilde{\Gamma}_{\mathfrak{R}}$ from $\tilde{p}_{\mathfrak{R}}$. The point $\tilde{p}_{\mathfrak{R}} + r_{\mathfrak{R}}\mathbf{v}_2$ is then a solution to the 2PBVP defined by (21) and the conditions

$$\mathbf{u}(1) \in \tilde{\Gamma}_{\mathfrak{R}}, \quad (22)$$

and

$$\mathbf{u}(0) \in \tilde{\Sigma}_{\mathfrak{R}} \quad (23)$$

for $T = 0$. An initial orbit segment, \mathbf{u} , on $W^s(C^3)$ with start point in \mathcal{L} is obtained by decreasing $\mathbf{u}(0)_A$ while also allowing integration time to increase in backwards time, corresponding to negative T . The continuation is stopped when $\mathbf{u}(0) \in \mathcal{L}$, in other words, when $\mathbf{u}(0)_A = 6.0$.

In the second step, we obtain an initial orbit segment on $W^u(C^2)$ with end point in \mathcal{L} through almost identical means. We consider the equilibrium $\hat{p}_{\mathfrak{R}}$ of (2) for $B = 0.4$ such that $(\hat{p}_{\mathfrak{R}_A}, 0.4, \hat{p}_{\mathfrak{R}_X}, \hat{p}_{\mathfrak{R}_Y}) \in C^2$ and the unstable eigenvectors \mathbf{k}_1 and \mathbf{k}_2 of $\hat{p}_{\mathfrak{R}}$. We then define $\hat{\Gamma}_{\mathfrak{R}} = \{\omega \in \mathbb{R}^3 \mid \hat{p}_{\mathfrak{R}} + r_{\mathfrak{R}}(\mathbf{v}_1 \sin(\theta) + \mathbf{v}_2 \cos(\theta)), \theta \in [0, 2\pi)\}$. The point $\hat{p}_{\mathfrak{R}} + r_{\mathfrak{R}}\mathbf{k}_2$ is then a solution to the 2PBVP defined by (21) and the conditions

$$\mathbf{w}(0) \in \hat{\Gamma}_{\mathfrak{R}} \quad (24)$$

and

$$\mathbf{w}(1) \in \hat{\Sigma}_{\mathfrak{R}}, \quad (25)$$

for $T = 0$. We increase $\mathbf{w}(1)_A$ while also allowing integration time to increase in forward time, corresponding to positive T . The continuation is stopped when $\mathbf{w}(1) \in \mathcal{L}$.

In the third step, we define the Lin vector

$$\mathbf{v}_Z = \frac{\mathbf{u}(0) - \mathbf{w}(1)}{\|\mathbf{u}(0) - \mathbf{w}(1)\|}, \quad (26)$$

that is three dimensional. We also define a normal vector $\mathbf{n} = (0, -\mathbf{v}_{Z_Y}, -\mathbf{v}_{Z_X})$ such that $\mathbf{n} \perp \mathbf{v}_Z$. We then define the conditions

$$\begin{aligned} \mathbf{u}(0), \mathbf{w}(1) &\in \mathcal{L} \\ (\mathbf{u}(0) - \mathbf{w}(1)) \cdot \mathbf{n} &= 0. \end{aligned} \quad (27)$$

To close the Lin gap, η we impose conditions (22), (24), and (27) while decreasing η and allowing integration time to move freely. The continuation is stopped when $\eta = 0$ at which point the concatenation of \mathbf{w} with \mathbf{u} forms an approximation of a heteroclinic connection on \mathcal{H}_0 . We can then sweep out the portion of \mathcal{H}_0 corresponding to real eigenvalues increasing and decreasing the parameter B inside the interval $(F_{2B}, 0.47685750162]$ while requiring that $\eta = 0$. We choose to stop our continuation at $B = 0.47685750162$, before the eigenvalues switch from real to complex conjugate. Unlike the computation of \mathcal{H} , the computational set up for \mathcal{H}^* allows us to decrease B past the value of q_B . We are thus able to compute the entire portion of \mathcal{H}_0 corresponding to real eigenvalues.

5.2. Complex conjugate eigenvalues

The method for computing an initial orbit segment, \mathbf{u} , on $W^s(C^3)$ for complex conjugate eigenvalues is similar except that throughout the computation and the definitions of associated surfaces, we substitute \tilde{p}_{\Re} for the equilibrium \tilde{p}_{\Im} of 2 for $B = 0.7$ such that $(\tilde{p}_{\Im_A}, 0.7, \tilde{p}_{\Im_X}, \tilde{p}_{\Im_Y})$.

The computation of orbit segments on $W^u(C^2)$ for B -values whose corresponding equilibria on C^2 that have complex conjugate eigenvalues presents the additional challenge. Namely, some orbit segments on $W^u(C^2)$ contain a segment that spirals tightly around C^2 while others do not. Orbit segments that spiral require larger mesh sizes than those that do not, however mesh size is held constant in our continuation. To address this issue, we define a radius $r_{\Im} = f(B)$, where $f(B)$ is the linear function such that $f(0.47685750164) = 0.0001$ and $f(0.86) = 0.2$. This allows us to avoid the tightly spiralling regions by choosing a start point farther away from C^2 in those areas.

To compute an initial orbit segment, \mathbf{w} , on $W^u(C^2)$, we begin by considering the equilibrium \hat{p}_{\Im} of (2) for $B = 0.7$ such that $(\hat{p}_{\Im_A}, 0.7, \hat{p}_{\Im_X}, \hat{p}_{\Im_Y}) \in C^2$. $\hat{\Sigma}_{\Im} = \{\omega \in \mathbb{R}^3 \mid \omega_Y = \hat{p}_{\Im_Y}\}$ and a one-dimensional circle $\hat{\Gamma}_{\Im} = \{\omega \in \mathbb{R}^3 \mid \hat{p}_{\Im} + f(0.7)(\mathbf{h}_1 \sin(\theta) + \mathbf{h}_2 \cos(\theta)), \theta \in [0, 2\pi]\}$ where \mathbf{h}_1 and \mathbf{h}_2 are the real and complex parts of the unstable complex conjugate eigenvectors of \hat{p}_{\Re} . The point $\hat{p}_{\Im} + f(0.7)\mathbf{h}_2$ then becomes a solution to the 2PBVP defined by (21) and the conditions

$$\mathbf{w}(0) \in \hat{\Gamma}_{\Im} \quad (28)$$

and

$$\mathbf{w}(1) \in \hat{\Sigma}_{\Im}, \quad (29)$$

for $T = 0$. To obtain a \mathbf{w} such that $\mathbf{w}(1) \in \mathcal{L}$, we increase $\mathbf{w}(1)_A$ while allowing T to increase and stop the continuation when $\mathbf{w}(1)_A = 6.0$.

We close the Lin gap by imposing the conditions (22), (26), and (28) while decreasing η and allowing integration to move freely. The continuation is stopped when $\eta = 0$ at which point the concatenation of \mathbf{w} with \mathbf{u} forms an approximation of a heteroclinic connection on \mathcal{H}_0 . We can then sweep out the portion of the manifold corresponding to complex conjugate eigenvalues by increasing and decreasing the parameter B inside the interval $[0.47685750164, H)$ while requiring that $\eta = 0$. We choose to stop the continuation at $B = 0.47685750164$ before the eigenvalues switch from complex conjugate to real.

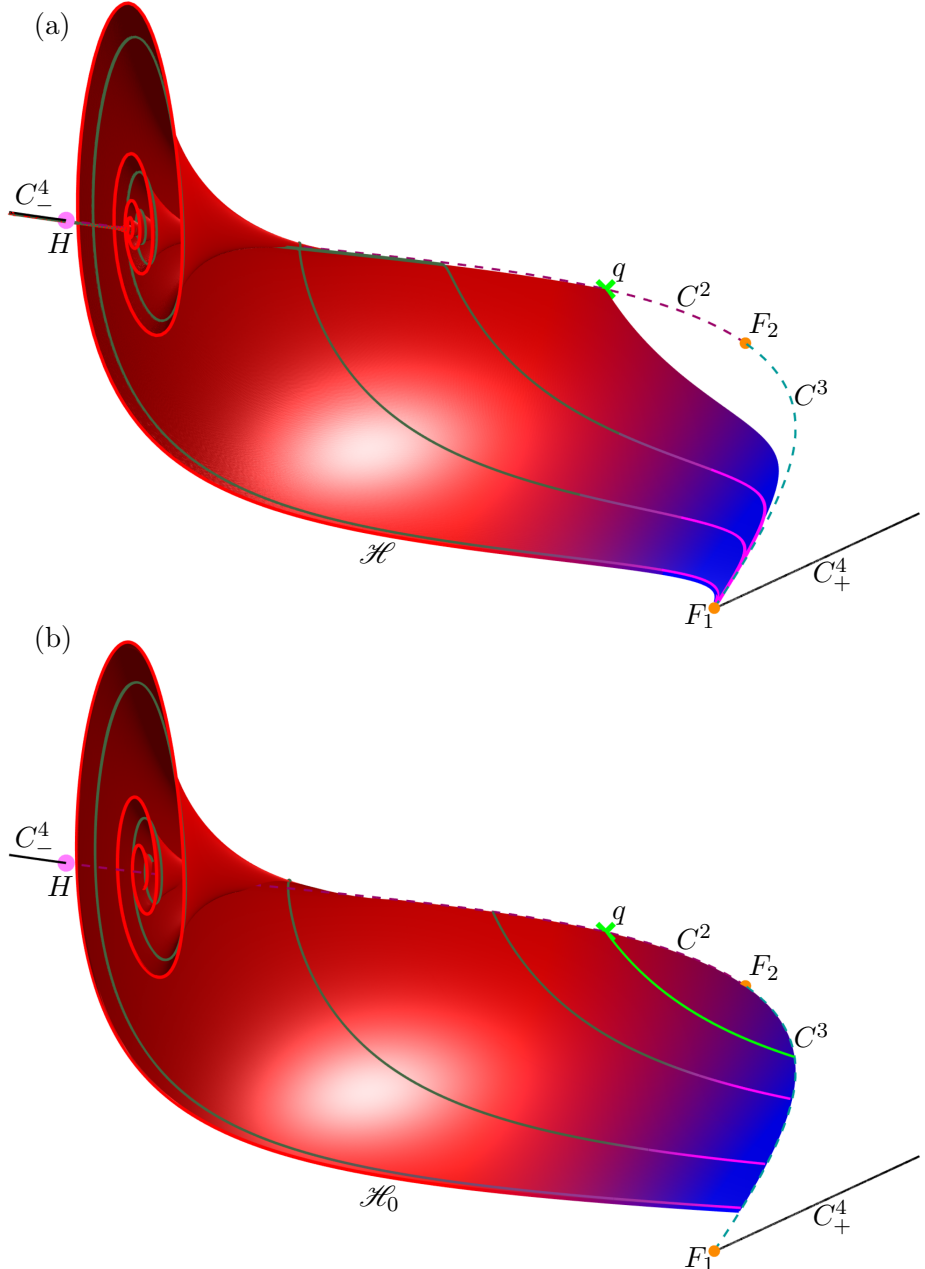


Fig. 11. Projections into (B, A, X) -space of (a) \mathcal{H} (red-blue fade) and (b) the portion of \mathcal{H}_0 lying in the region $B < 0.781$ (red-blue fade). Representative orbit segments are plotted fading from forest green to magenta. The intersection of the singular unstable manifold of q is plotted in (b) as a green orbit segment on \mathcal{H}_0 . The critical manifold is also shown.

Figure 11 shows \mathcal{H}_0 projected into (B, A, X) - and (B, A, Y) -space. For visual comparison with \mathcal{H} , we show only the portion of \mathcal{H}_0 that lies in the region $B < 0.781$. The computational set up is not visualized in figure 11 and the color of \mathcal{H}_0 fades from red to blue in colouring to illustrate its non-dependence on our choice of \mathcal{L} .

5.3. Distance from \mathcal{H}

We analyse the difference between \mathcal{H} and \mathcal{H}_0 using the integral norm to measure the distance between intersection curves of \mathcal{H} and \mathcal{H}_0 with different subspaces of the phase space defined by constant values of B .

6. Implications for mixed-mode oscillation geometry

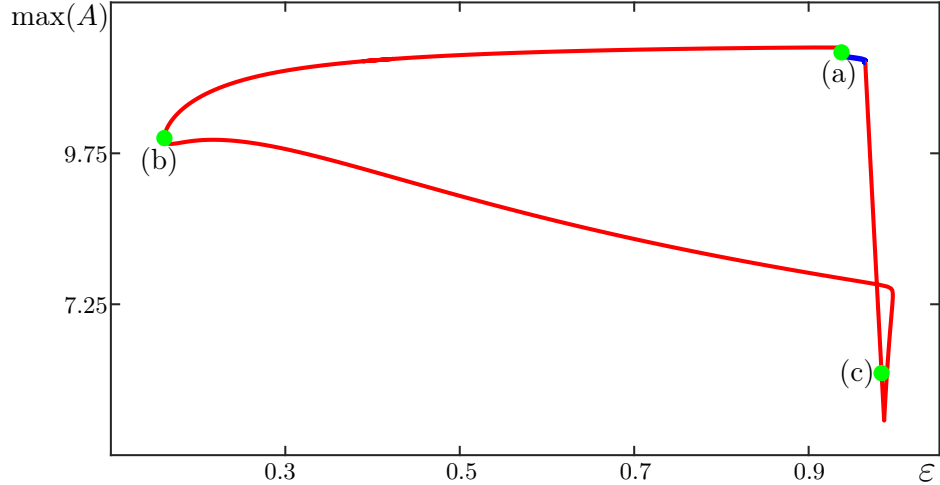


Fig. 12. The isola of MMs for different values for ε . The segment of the isola on which Γ is unstable is plotted in red and the much smaller segment on which Γ is stable is plotted in blue. Green dots labeled (a), (b), and (c) correspond to MMs shown in Figure 14.

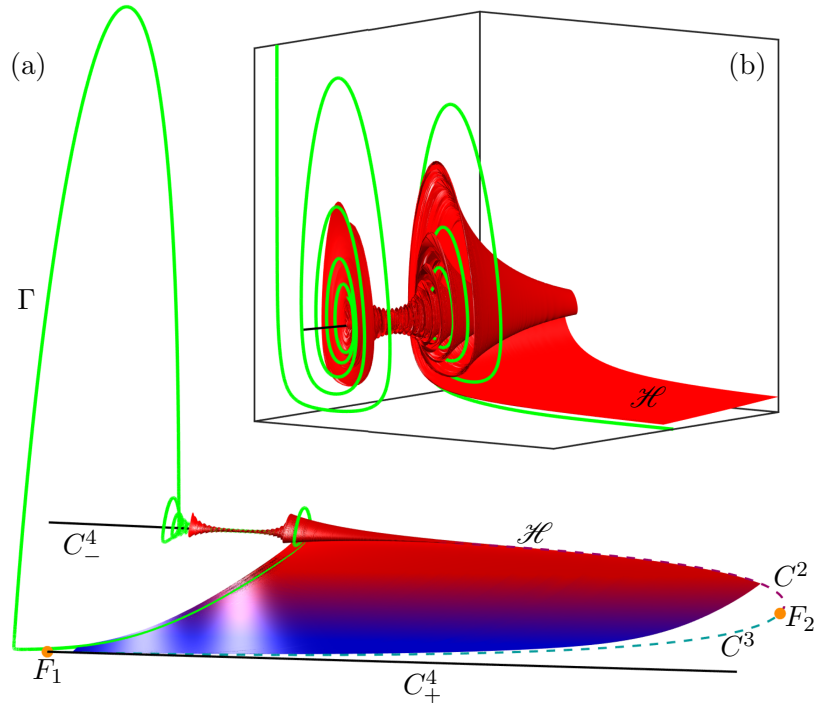


Fig. 13. The surface of heteroclinic connections \mathcal{H} (red-blue fade) is extended in backwards time and projected into (B, A, X) -space. The MMO of interest Γ (green) and the critical manifold are also plotted in the (B, A, X) -space. The global view (a) shows Γ tracking \mathcal{H} from the region of SAOs near C^2 to C^3 . The MMO passes F_1 and makes a single LAO. The LAO ends at the stable branch C_-^4 and enters the region of SAOs via the spiralling region of \mathcal{H} . An enlargement of Γ entering the spiralling region of \mathcal{H} is shown in inlay (b). The MMO makes a slow passage through the Hopf point H before exiting the region of SAOs.

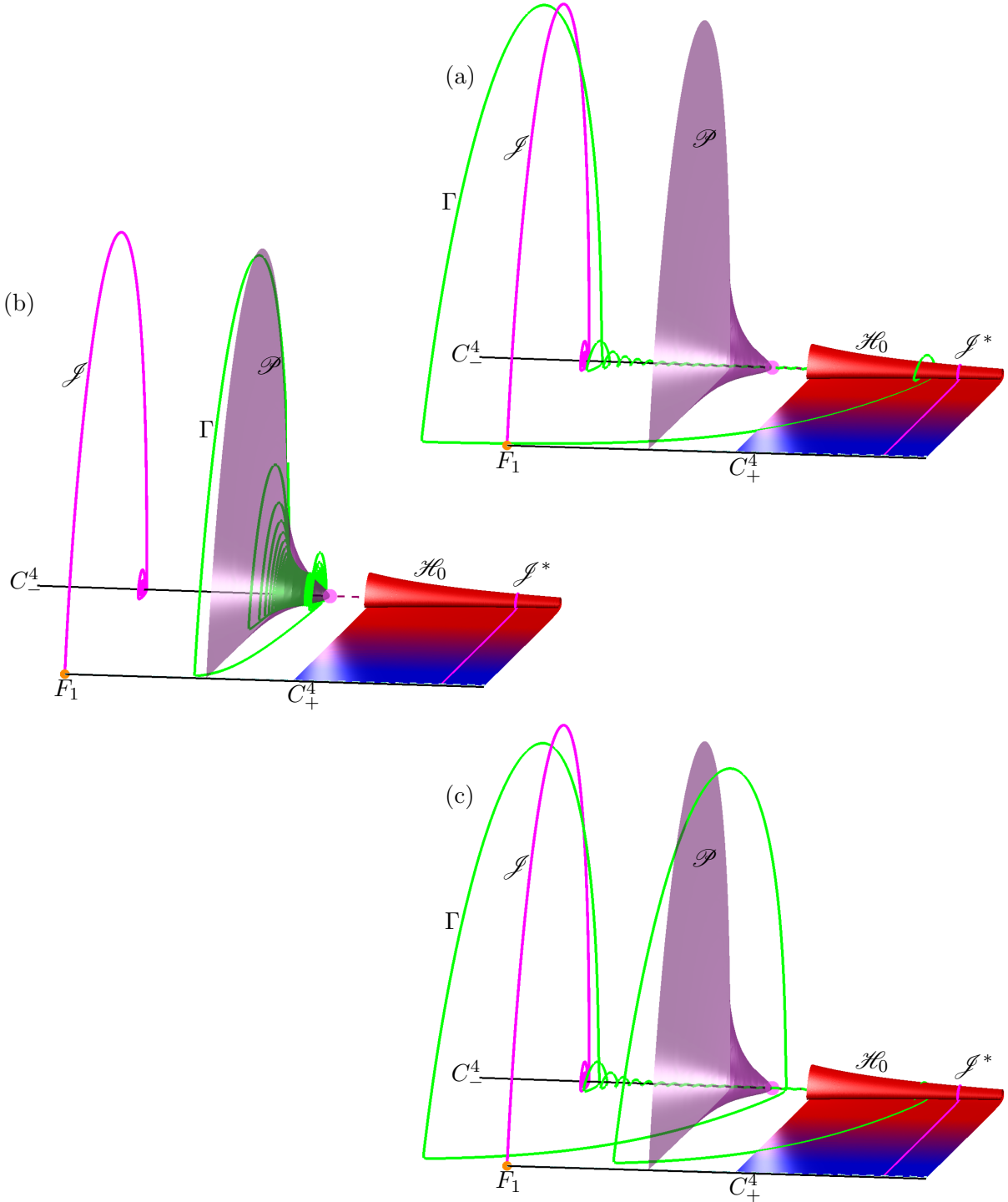


Fig. 14. In panels (a), (b), and (c) the singular surface \mathcal{H}_0 (red-blue fade) is projected into (B, A, X) -space with several other singular objects. The jump back trajectory \mathcal{J} and its dual \mathcal{J}^* are plotted in magenta. The surface of singular POs \mathcal{P} is plotted in midnight grape. Panel (a) shows Γ for the original value of $\varepsilon = 0.0037$ corresponding to the green dot labeled (a) in Figure 13. The MMO's entry and exits from the region of SAOs track \mathcal{J} and \mathcal{J}^* . Panel (b) shows Γ for $\varepsilon = 5.45544 \times 10^{-4}$, corresponding to the rightmost fold of the isola, shown as a green dot in Figure 13 and labeled (b). This Γ tracks \mathcal{P} and enters the region of SAOs via a homoclinic connection of a saddle equilibrium of (2) lying on C^3 . The MMO exits the region of SAOs before reaching C^2 . Panel (c) shows Γ for $\varepsilon = 0.00383456$ corresponding to the green dot shown in Figure 13 labeled (c). The MMO is very similar to the Γ shown in (a) with the exception that it makes an additional large amplitude to C^2 before returning to the region of SAOs.

We investigate the interaction between the MMO and \mathcal{H} and \mathcal{H}_0 respectively for varying ε . We consider the original MMO of interest corresponding to the original value $\varepsilon = 0.0037$ as well as MMOs corresponding to $\varepsilon = 0.0038$ and $\varepsilon = 0.0005$. These are representative MMOs of different type within the MMO parameter regime. For the original MMO, we consider the effect of the surface \mathcal{H} and then explore the singular objects, including \mathcal{H}_0 , that also affect the geometry. For the MMOs corresponding to $\varepsilon = 0.0038$ and $\varepsilon = 0.0005$ we only consider the singular objects that organize the MMO geometry. Our analysis in section 5.3 shows that the difference between \mathcal{H} and \mathcal{H}_0 is minimal and so it is reasonable to only consider \mathcal{H}_0 for MMOs corresponding to small ε .

Figures ??(a) and (b) show (B,A,X) - and (B,A,Y) -projections of the mixed-mode oscillation, neon green, plotted with \mathcal{H} , red to blue fade. In this figure, we have extended \mathcal{H} so that $\mathbf{u}(0)_B = \mathbf{w}(1)_B = 0.8724$. This facilitates comprehension of the MMO's entry into the region of SAOs, although it obscures some of the geometry of \mathcal{H} . The surface serves as a reinjection mechanism from the region of SAOs into the region of LAOs. The MMO begins near C_-^4 and spirals as it passes through the H point to C^2 . The distance in B between H and the MMO's exit from the region of SAOs is approximately the same as the distance in B between the MMO's entry and H . After exiting the region of SAOs, the MMO traverses \mathcal{H} to reach C^3 . The MMO follows C^3 and then makes a large, fast excursion mostly in the X and Y directions before being attracted back to C_-^4 again. Shown in the inlays are enlargements of the region of SAOs. In these enlargements, we see the details of the scrolling region of \mathcal{H} and the slow passage of the MMO through the Hopf bifurcation.

Figure ??(a) and (b) show (B,A,X) - and (B,A,Y) - projections of an enlargement of the original MMO with several singular objects. The singular surface of heteroclinic connections \mathcal{H}_0 is plotted fading from red to blue. The jump back trajectory, plotted in magenta, is the trajectory in 2 that connects F_1 to the equilibrium of (2) for $B = F_{1B}$ lying on C_-^4 . The jump trajectory's dual is the trajectory lying on \mathcal{H}_0 that is at the same distance from H with respect to B as the jump trajectory. A surface of saddle periodic orbits (POs) of system (2) is plotted in midnight grape. These originate from H and terminate in a homoclinic connection of an equilibrium of (2) lying on C^3 . The MMO's entry into and exit from the region of SAOs remain close to the jump orbit and its dual respectively. A significant amount of drift in the B direction can be seen in the MMO away from the slow manifolds. Figure ??(c) shows an isola in parameter space that the MMO lies on. The horizontal axis indicates the value of ε and the vertical axis indicates the maximum value of the variable A on the MMO. Red curves indicate where the MMO has at least one unstable Floquet multiplier while blue curves indicate where the MMO is stable. The location of the MMO on the isola is indicated with a green dot and signifies that the original MMO is stable.

Figure ??(a) and (b) show (B,A,X) - and (B,A,Y) -projections of a zoom of the MMO for $\varepsilon = 0.0005$ with the singular objects described above. The MMO, plotted in neon green, remains close to the surface of singular POs. The MMO enters the region of SAOs via the homoclinic connection of the equilibrium lying on C^3 and the SAOs track the interior of the surface of singular POs in the (B,A,X) - and (B,A,Y) -projections. The MMO exits the region of SAOs by passing through the surface of singular POs in the (B,A,X) - and (B,A,Y) -projections and then being repelled away from it. Figure ??(a) shows the location of the MMO on the leftmost fold of the isola.

Figure ??(a) and (b) show (B,A,X) - and (B,A,Y) -projections of a zoom of the MMO for $\varepsilon = 0.0005$ with the singular objects described above. Similarly to the MMO at $\varepsilon = 0.0037$, the SAOs for the MMO at $\varepsilon = 0.0038$ are due to a slow passage through H . The entry and exits from the region of SAOs are close to the jump trajectory and its dual. An early return to C^2 occurs between the MMO's exit and reentry into the region of SAOs. This MMO differs from the other MMOs discussed as it has two LAOs instead of one. Figure ??(c) shows the location of the MMO at $\varepsilon = 0.0038$ on the isola, near to the rightmost fold.

References

- Benoît, E. [1982] “Systèmes lents-rapides dans \mathbb{R}^3 et leurs canards,” *Proceedings of the Third Schnepfenried Geometry Conference* **2**, 159–191.
- Benoît, E. [1985] “Enlacements de canards,” *Comptes Rendus Mathematique Academie des Sciences* **300**, 225–230.
- Benoît, E., Callot, J. F., Diener, F. & Diener, M. [1981] “Chasse au canard,” *Collectanea Mathematica* **31**, 37–119.
- Brøns, M. & Bar-Eli, K. [1991] “Canard explosion and excitation in a model of the Belousov-Zhabotinskii reaction,” *Journal of Physical Chemistry A* **95**, 8706–8713.
- Brøns, M., Krupa, M. & Wechselberger, M. [2006] “Mixed mode oscillations due to the generalized canard phenomenon,” *Fields Institute Communications* , 39–63.
- De Maesschalck, P. & Wechselberger, M. [2015] “Neural Excitability and Singular Bifurcations.” *The Journal of Mathematical Neuroscience* **5**.
- Desroches, M., Guckenheimer, J., Krauskopf, B., Kuehn, C., Osinga, H. & Wechselberger, M. [2012] “Mixed-Mode Oscillations with Multiple Time Scales.” *SIAM Review* **54**, 211–288.
- Desroches, M., Krauskopf, B. & Osinga, H. [2009] “The geometry of mixed-mode oscillations in the Olsen model for peroxidase-oxidase reaction.” *Discrete & Continuous Dynamical Systems* **2**, 807–827.
- Doedel, E. [2007] *AUTO-07p: Continuation and Bifurcation Software for Ordinary Differential Equations*, URL <http://indy.cs.concordia.ca/auto/>, with major contributions from A.R. Champneys, F. Dercole, T.F. Fairgrieve, Y.A. Kuznetsov, R.C. Paffenroth, B. Sandstede, X. Wang and C. Zhang.
- Farjami, S., Kirk, V. & Osinga, H. [2018] “Computing the Stable Manifold of a Saddle Slow Manifold.” *SIAM Journal on Applied Dynamical Systems* **17**, 350–379.
- Fenichel, N. [1979] “Geometric singular perturbation theory for ordinary differential equations,” *Journal of Differential Equations* **31**, 53–98.
- FitzHugh, R. [1955] “Mathematical models of threshold phenomena in the nerve membrane,” *The bulletin of mathematical biophysics* **17**, 257–278.
- Guckenheimer, J. [1985] “Singular hopf bifurcation in systems with two slow variables,” *SIAM Journal on Applied Dynamical Systems* **7**, 1355–1377.
- Háro, A. & de la Liave, R. [2006] “A parameterization method for the computation of invariant tori and their whiskers in quasi-periodic maps: Rigorous results,” *Journal of Differential Equations* **228**, 530–579.
- Harvey, E., Kirk, V., Osinga, H., Sneyd, J. & Wechselberger, M. [2010] “Understanding anomalous delays in a model of intracellular calcium dynamics,” *Chaos: An Interdisciplinary Journal of Nonlinear Science* **20**.
- Hasan, C., Krauskopf, B. & Osinga, H. [2018] “Saddle slow manifolds and canard orbits in \mathbb{R}^4 and application to the full hodgkin-huxley model,” *Journal of Mathematical Neuroscience* **8**.
- Hudson, J. L., Hart, M. & Marinko, D. [1979] “An experimental study of multiple peak periodic and nonperiodic oscillations in the Belousov-Zhabotinskii reaction,” *The Journal of Chemical Physics* **71**, 1601–1606.
- Jorba, A. & Olmedo, E. [2009] “On the computation of reducible invariant tori on a parallel computer,” *SIAM Journal on Applied Mathematics* **8**, 1382–1404.
- Krauskopf, B., Osinga, H. & Galán-Vioque [2007] *Numerical continuation methods for dynamical systems* (Springer International Publishing).
- Krauskopf, B. & Rieß, T. [2008] “A lin’s method approach to finding and continuing heteroclinic connections involving periodic orbits,” *Nonlinearity* **21**, 1655–1690.
- Krupa, M., Popović, N. & Kopell, N. [2008] “Mixed-mode oscillations in three time-scale systems: A prototypical example,” *SIAM Journal on Applied Dynamical Systems* , 361–420.
- Kuehn, C. & Szmolyan, P. [2015] “Multiscale Geometry of the Olsen Model and Non-classical Relaxation Oscillations.” *Journal of Nonlinear Science* **25**, 583–629.
- Lin, X. [1989] “Shadowing lemma and singularly perturbed boundary value problems,” *SIAM Journal of Applied Mathematics* **49**, 26–54.

- Mitry, J., McCarthy, M., Kopell, N. & Wechselberger, M. [2013] “Excitable neurons, firing threshold manifolds and canards,” *The journal of mathematical neuroscience* **3**.
- Olsen, L. [1983] “An enzyme reaction with a strange attractor.” *Physics Letters A* **94**, 454–457.
- Otto, C., Ludge, K., Vladimirov, A. G., Wolfrum, M. & Scholl, E. [2012] “Delay-induced dynamics and jitter reduction of passively mode-locked semiconductor lasers subject to optical feedback,” *New Journal of Physics* **14**.
- Piltz, S. H., Veerman, F., Maini, P. K. & Porter, M. A. [2017] “A predator–2 prey fast–slow dynamical system for rapid predator evolution,” *SIAM Journal on Applied Dynamical Systems* **16**, 54–90.
- Rockafellar, R. T. & Wets, R. J.-B. [2009] *Variational Analysis*, 3rd ed. (Springer International Publishing).
- Van der Pol, B. [1927] “Forced oscillations in a circuit with non-linear resistance. (Reception with reactive triode).” *The London, Edinburgh, and Dublin Philosophical Magazine and Journal of Science* **3**, 65–80.
- Vo, T., Bertram, R. & Wechselberger, M. [2013a] “Multiple geometric viewpoints of mixed mode dynamics associated with pseudo-plateau bursting,” *SIAM Journal on Applied Dynamical Systems* **12**.
- Vo, T., Tabak, J., Bertram, R. & Wechselberger, M. [2013b] “A geometric understanding of how fast activating potassium channels promote bursting in pituitary cells,” *Journal of Computational Neuroscience* **36**.
- Waalkens, H., Burbanks, A. & Wiggins, S. [2005] “A formula to compute the microcanonical volume of reactive initial conditions in transition state theory,” *Journal of Physics A: Mathematical and General* **38**, L759–L768, URL <http://stacks.iop.org/0305-4470/38/i=45/a=L03>.
- Zhang, W., Krauskopf, B. & Kirk, V. [2012] “How to find a codimension-one heteroclinic cycle between two periodic orbits,” *Discrete and Continuous Dynamical Systems* **32**, 2825–2851.